Inline Motion in Flapping Foils for Improved Force Vectoring Performance

by

Jacob Izraelevitz

Submitted to the Department of Mechanical Engineering
in partial fulfillment of the requirements for the degree of

Master of Science in Mechanical Engineering

at the

MASSACHUSETTS INSTITUTE OF TECHNOLOGY

September 2013

Author .....
Department of Mechanical Engineering
August 31, 2013

Certified by .....
Michael Triantafyllou
Professor of Mechanical and Ocean Engineering
Thesis Supervisor

Accepted by .....
David E. Hardt, Professor of Mechanical Engineering
Chairman, Department Committee on Graduate Theses

Inline Motion in Flapping Foils for Improved Force Vectoring Performance

by

Jacob Izraelevitz

Submitted to the Department of Mechanical Engineering
on August 31, 2013, in partial fulfillment of the
requirements for the degree of
Master of Science in Mechanical Engineering

Abstract

In this thesis, I study the effect of adding in-line oscillation to heaving and pitching foils using a power downstroke. I show that far from being a limitation imposed by the muscular structure of certain animals, in-line motion can be a powerful means to either substantially augment the mean lift, or reduce oscillatory lift and increase thrust. Additionally, I show that the use of a model-based optimization scheme, driving a sequence of experimental runs, allows the ability for flapping foils to tightly vector and keep the force in the desired direction, hence improving locomotion and maneuvering. I employ Particle Image Velocimetry (PIV) to visualize the various wake patterns of these foil trajectories and a force transducer to evaluate their performance within a towing-tank experiment.

Thesis Supervisor: Michael Triantafyllou
Title: Professor of Mechanical and Ocean Engineering

Acknowledgments

Principally, I would like to thank my advisor Professor Michael Triantafyllou for his valuable guidance throughout my graduate studies. Professor Gabriel Weymouth also acted as an additional voice of experience in hydrodynamics and provided access to his Lilypad CFD code.

Additionally, my lab group in the MIT Towing Tank Group gave thoughtful feedback, both in official meetings and over innumerable lunches: Heather Beem, Jeff Dusek, Audrey Maertens, Haining Zheng, James Schulmeister, Amy Gao, Stephanie Steele, and Dilip Thekkoodan. Heather, Jeff, and Stephanie were especially patient, teaching me how to conduct experiments in the Towing Tank while putting up with my questions and mistakes.

This project was partly developed through a collaboration with the SMART-CENSAM institute in Singapore, and our colleagues there also supported me and allowed use of their facilities.

I am also indebted to my friends and family, who helped me when I needed it most. My parents Terry and David, and brothers Joe and Adam, were always understanding and willing to listen.

And a special thanks goes to Leah Mendelson, who did an amazing job both keeping me sane off-campus and sometimes debugging my research on-campus.

Contents

List of Figures

List of Tables

Chapter 1

Introduction

Most fast-swimming fish undulate their caudal fins in a symmetric fashion, with equal force generation from both the upstroke and downstroke of the fin. In contrast, other animals such as turtles and birds, flap their fins and wings in an asymmetrical fashion. This asymmetry typically involves a powerful downstroke with large fluid forces and a 'feathering' upstroke with little force. Additionally, the flapping motion of the fin or wing is not purely transverse to the direction of motion of the animal, but also involves a strong oscillatory component parallel to its motion.

1.1 Biological Examples of In-Line Motion

There are major differences in how the in-line component is employed in different animals: In turtle swimming, the flipper is moved both perpendicular to the flow, as in a traditional symmetric flap, but also substantially parallel to the flow in the downstream direction (Fig. 1-1). This behavior has been noted in unrestrained swimming turtles, such as *Chelonia mydas* [4, 15], and also in mollusk labriform swimmers such as *Clione limacina* [29]. The significant motion parallel to the flow, or *in-line motion* [15], rotates the instantaneous flow over the flipper, orienting the downstroke lift to produce thrust rather than a transverse force. In addition, the angle of attack profile is further varied to obtain a powerful downstroke and weaker upstroke, creating a highly asymmetric flap that averages to a net thrust with little

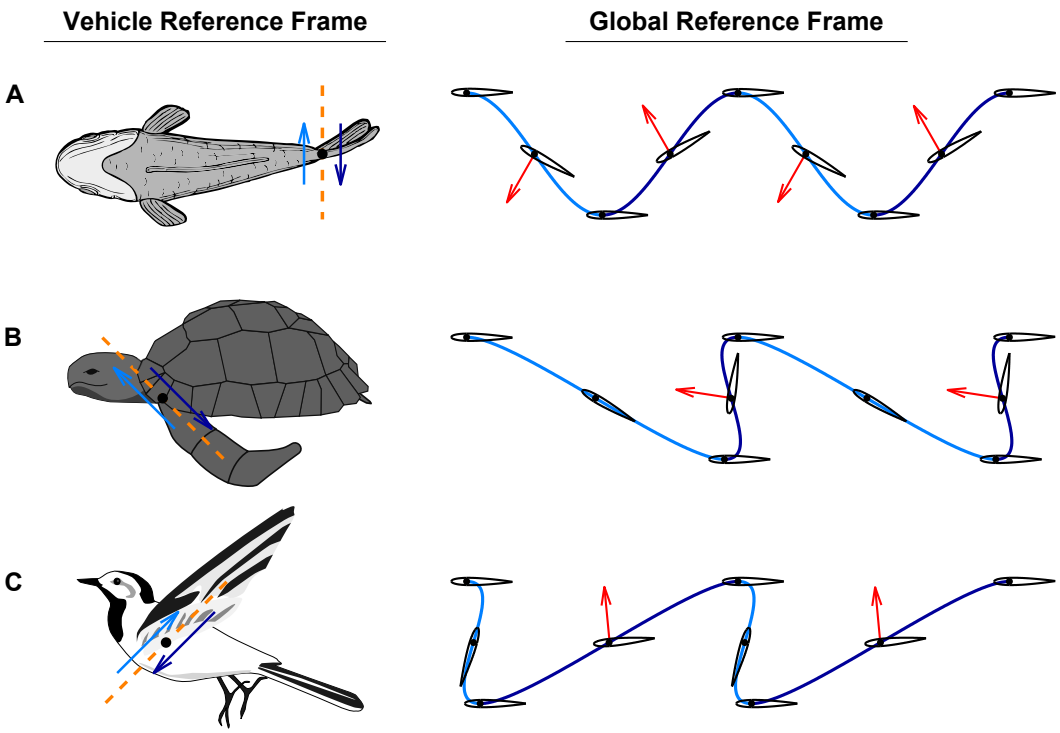

Figure 1-1: *Comparison of Symmetric, Forward In-line, and Backwards In-line* - Various biological examples are able to change the direction of flapping foil force, simply by changing the orientation of flapping relative to oncoming flow. This degree of freedom, the stroke angle, is usually ignored in experimental flapping foil studies, where the foil is constrained to flap only perpendicular to the flow.

instantaneous transverse force. Previous experiments in Licht et al. [15] have found that this mode of actuation generates less thrust, but can actually improve efficiency while mitigating the transverse force oscillation.

Birds also exhibit significant in-line motion, but instead direct their flaps forwards during the power downstroke, i.e. in the upstream direction (Fig. 1-1), thus augmenting the transverse force. Tobalske and Dial note that pigeons, magpies, and hummingbirds control their in-line motion as a function of airspeed, which they define using a stroke angle [34, 33]. Substantial upstream in-line motion helps support the weight of the bird at low speed; however, at high speeds the in-line motion is reduced since weight is constant while lift scales with the square of velocity [33]. In-line motion also varies strongly with flight speed in bats [16], a group with a very different evolutionary history than birds.

1.2 Experimental Flapping Foil Actuators

Symmetrically flapping foil actuators, inspired by animal flight and swimming, can be used to generate both thrust and lift, and can be hydrodynamically efficient; experiments have reported thrust efficiencies up to 80% [1, 22]. Introducing a bias in the angular motion causes the development of steady lift, in addition to thrust, hence enabling maneuvers [23, 27]. The oscillatory transverse forces that develop due to the unsteady flapping motion, however, constitute a disadvantage of such propulsors, in analogy to the rolling moment and breaking of symmetry introduced by rotating propellers.

Licht et al. [15] showed that in the case of a turtle, the in-line oscillatory motion causes the fin force to have a large in-line component and a small transverse component, which is ideally-suited for a neutrally buoyant animal in order to minimize transverse oscillations. Equally important, it was shown that its propulsive efficiency is equal or better than that for a symmetrically flapping foil (without in-line oscillatory motion).

Licht et al. [15] showed further in bird-like flapping, the inline motion during the powerstroke is in the opposite direction than that of the turtle, which results in substantially increased lift and serves to support the weight of the bird. As noted already, as the forward speed increases, a bird reduces the amplitude of its in-line motion, because the lift force scales with the square of the speed while its weight remains constant.

Hence, the added complexity of superposing an in-line oscillatory motion to a flapping foil is compensated by the ability to better control the direction of the produced forces to suit the function of the particular animal, without sacrificing propulsive efficiency. Such directional control ability is also very important for maneuvering, especially when the animal must execute a sharp change of direction. In contrast, a symmetrically flapping foil always produces large transverse oscillatory forces, whose effect may be reduced by averaging out when in steady translation, but not when in transient motion, thus posing serious limitations in force direction control.

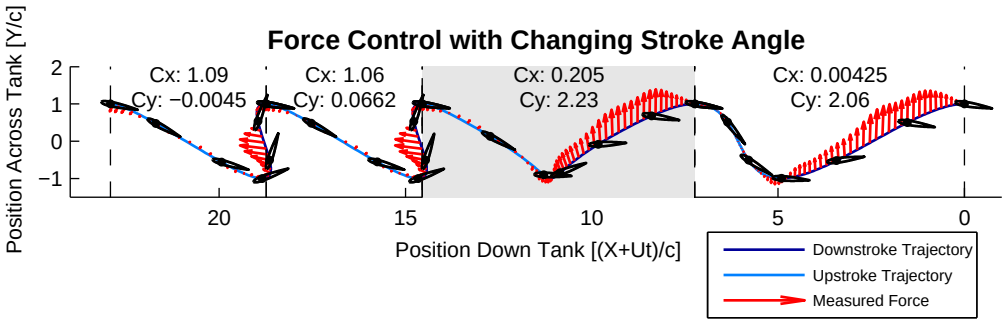

Figure 1-2: *Using the Stroke Angle for Force Control* - Experimentally measured force profile of a maneuver where the stroke angle is changed from a bird-like trajectory with a large transverse force coefficient C_y, to a turtle-like trajectory with all in-line force C_x. The instantaneous fluid force on the foil is indicated by the red arrows, while the transition flapping cycle is indicated by the gray region. Averaged over 8 trials, filtered at 5 Hz with a 5th order low-pass Butterworth filter, as described in Chapter 3.

Fig. 1-2 illustrates an example of a changing stroke angle to improve the force performance of a flapping foil. In this experiment, the foil is oscillated upstream during the first downstroke, and downstream during the third and fourth downstrokes. The mean force coefficients change from a large transverse force to all in-line force, using a single transition cycle to smooth the different motion trajectories. Such a control scheme could be used on a flapping foil vehicle to provide augmented maneuverability on the timescale of individual flapping cycles.

In this thesis I explore the possibility of enabling tight force control through optimization of the in-line motion of asymmetrically flapping foils. I show through a series of experiments on a high aspect ratio foil that both thrust and lift force can be controlled through in-line motion optimization. The use of active motion control can further enhance the performance of asymmetrically flapping foils, hence providing a prime means for tight force control that can significantly improve maneuverability.

1.3 Chapters Overview and Trajectory Descriptions

I explore the effect of the in-line motion parameters, starting with the symmetrically flapping foil and then proceeding with various shapes of in-line forcing, emulating the flapping motions of birds and turtles. I present results in detail of seven different motion trajectories, enumerated in Table 1.1.

Trajectory Name	Stroke Angle	Strouhal Number	AoA Profile
Trajectory I No In-line Motion	$\beta = 90°$	$St = 0.3$	Sinusoid - max 25°
Trajectory II Upstream In-line	$\beta = 45°$	$St = 0.3$	Cosinusoid - max 25°
Trajectory III Downstream In-line	$\beta = 135°$	$St = 0.3$	Cosinusoid - max 25°
Closed-Loop IIIb Downstream In-line	$\beta = 135°$	$St = 0.3$	Closed-Loop Control
Optimized IV Mean Cx=1 Cy=0	$\beta = 135°$	$St = 0.48$	Optimized
Optimized V Mean Cx=0 Cy=2	$\beta = 57°$	$St = 0.28$	Optimized
Optimized VI Mean Cx=1 Cy=4	$\beta = 59°$	$St = 0.5$	Optimized

Table 1.1: Motion Trajectories

Chapter 2 gives a historical overview of the fundamental fluid dynamics of flapping foils. The chapter briefly covers potential flow, foils, delayed stall effects, and unsteady foil theory.

Chapter 3 explains the experimental apparatus used to test these in-line motion flaps, located in the MIT Towing Tank laboratory. These experiments measure the force and moments generated by the flapping foil, as well as visualize the wake using Particle Image Velocimetry (PIV). This chapter also describes the motion definition of the foil trajectory, as well as the different metrics used to judge the quality of the foil force performance.

Chapter 4 details the experimental results from the first three trajectories in Table

1.1. These three trajectories give an initial pass on the utility of in-line motion, as well as the necessity of additional techniques to mitigate unwanted forces from unsteady fluid effects.

Chapter 5 illustrates one solution to mitigating unwanted fluid forces, using a control scheme to change the foil angle of attack to remove the force disturbances. The control solution is implemented in a CFD solver developed by Weymouth et al. [39]. The control solution does successfully mitigate the unwanted fluid forces; however, implementing a real-time control in the actual experiment was deemed unfavorable when compared to an optimization-based design approach. This chapter discusses the force performance of Trajectory IIIb, a force-controlled version of the experimental Trajectory III (Table 1.1).

Chapter 6 gives an overview of an optimization routine used to design in-line motion trajectories with excellent force performance without the need for a real-time controller. The optimization employs a nonlinear fluids model, using the SNOPT algorithm developed by Gill et al. [7].

Chapter 7 illustrates how the optimization routine can be used to make incremental corrections on experiment results, using the theoretical model developed in Chapter 6. Three flapping trajectories, Optimized IV, V, and VI from Table 1.1, are designed using this method. The force performance of these final trajectories are discussed, along with visualizations from their wakes.

Chapter 8 concludes the thesis and places the results of the optimization routine back into the larger context of flapping foils.

Chapter 2

2D Unsteady Foil Theory Background

This chapter goes over the fundamental theory of unsteady foils in potential flow, along with more recent developments in flapping foil propulsors.

2.1 Potential Flow

The classic Navier-Stokes equation governing fluid flow describes the forces on a point in the fluid, essentially acting as Newton's Second Law:

$$\rho\left(\frac{\partial \mathbf{v}}{\partial t} + \mathbf{v}\cdot\nabla\mathbf{v}\right) = -\nabla p + \mu\nabla^2\mathbf{v} + F_g \tag{2.1}$$

Where $\mathbf{v}$ is the fluid velocity vector at a fixed point in space, ρ is the fluid density, p is the pressure, μ is the fluid viscosity, and F_g is the gravitational force. The left side indicates the acceleration of the fluid, while the right side indicates the three main forces: a pressure (or inertia) force, a frictional force from viscosity, and gravity.

In most subsonic foil problems, the fluid is modeled as incompressible, meaning that the divergence of the velocity vector must be zero to conserve mass:

$$\nabla\cdot\mathbf{v} = 0 \tag{2.2}$$

Additionally, for most applications of foils, the Reynolds number is much larger than 1, usually on the order of multiple thousand:

$$Re = \frac{\rho U L}{\mu} \gg 1 \tag{2.3}$$

The Reynolds number gives an approximation of how important the pressure term is compared to the friction term in the Navier-Stokes Equation (Eqn 2.1). We can therefore ignore the viscous term $\mu\nabla^2\mathbf{v}$, leading to *ideal flow* theory. In these problems, the viscous term is only important very near the foil, in the boundary layer first predicted by Prandtl. The Navier-Stokes equation, once such simplified, becomes linear and much easier to solve.

We can now recharacterize the flow velocity as the gradient of a new scalar field ϕ called the *flow potential*, where:

$$\begin{aligned} \mathbf{v} &= \nabla\phi \\ \nabla^2\phi &= 0 \end{aligned} \tag{2.4}$$

Since the problem is now linear, the sum of any two solutions is also a solution to the fluid equations. We can therefore represent a foil in flow as the sum of a set of fundamental flows. One example fundamental flow is the *point source*:

$$\phi(r,\theta) = \frac{m}{2\pi}\ln r \tag{2.5}$$

This fundamental flow is fluid diverging from a single point of source strength m, where r is the radius from the point. In general, bodies are represented in a fluid as a collection of positive and negative point sources.

An additional important fundamental flow is the *point vortex*:

$$\phi(r,\theta) = \frac{\Gamma}{2\pi}\theta \tag{2.6}$$

This fundamental flow is a point of rotating fluid, or a vortex, of circulation strength Γ. In truly ideal flow, a vortex is a single point, but viscous effects actually diffuse

the vortex. The circulation is defined as area integral of the vorticity ω:

$$\begin{aligned} \omega &= \nabla \times \mathbf{v} \\ \Gamma &= \int_A \omega dA = \oint_C \mathbf{v} \cdot dS \end{aligned} \tag{2.7}$$

An interesting consequence of potential flow is that the force on a body made of point sources and sinks in a steady flow is exactly zero, meaning that this formulation cannot predict the drag on a body. The drag is caused by viscous affects - both friction in the boundary layer and flow separation that develops out of this boundary layer, neither of which is predicted by the ideal flow theory. However, there is a lifting force on a vortex:

$$L = -\rho U \Gamma \tag{2.8}$$

Where U is the velocity of the flow relative to the vortex (2D formulation).

Additionally, potential flow also predicts the added mass on a body, or the fluid force from accelerating a region of fluid along with an accelerating body.

2.2 Foils and the Kutta Condition

The airfoil in potential flow is a collection of point sources and sinks, arranged such that the boundary condition takes the classic shape of an airfoil. However, the solution with only these point sources and sinks creates an infinite velocity at the trailing edge of the foil, as the fluid whips around the sharp edge (Figure 2-1).

A foil will therefore develop a net circulation Γ, represented by point vorticies within the body, that mitigates this infinite velocity. This is called the Kutta Condition, and explains why foils must have a sharp trailing edge in order to generate lift. The foil lift is therefore proportional to the *bound circulation* of the foil, which only exists because of the sharp trailing edge.

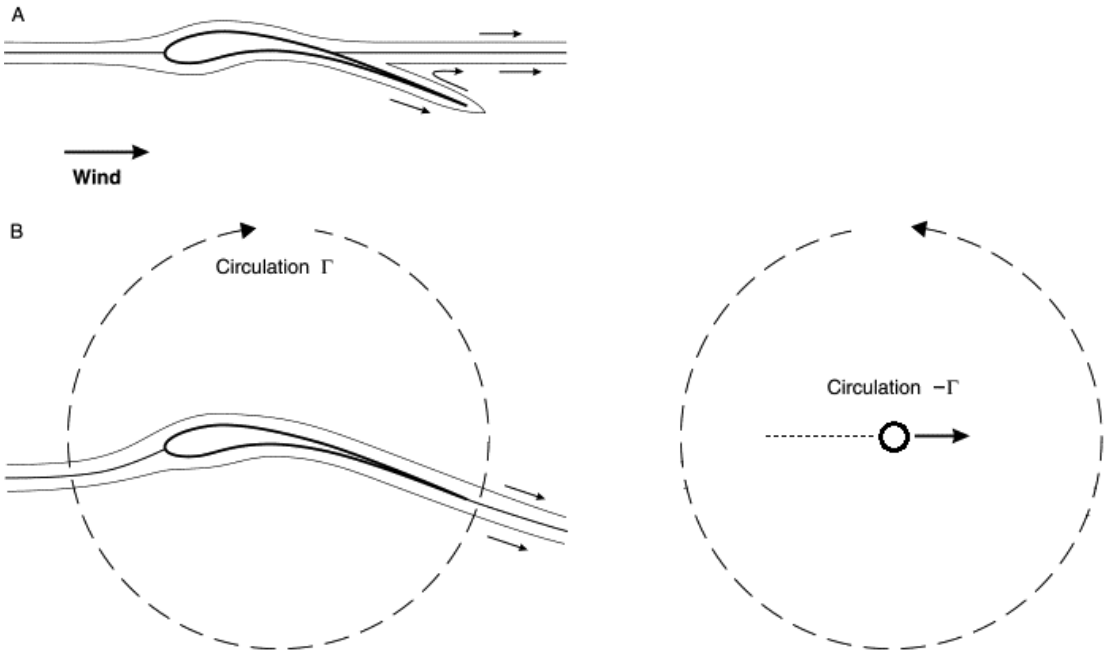

Figure 2-1: *Kutta Condition and Wake Vorticity* - An airfoil has some *bound* circulation to enforce the Kutta condition at the trailing edge. Any bound circulation must be accounted for by vortices in the wake of opposite circulation (adapted from [21]).

2.3 Foil Flutter

A consequence of the generation of bound circulation is the creation of additional vortices in the wake of the opposite sign, often called trailing edge vortices (TEVs). Kelvin's Theorem states the circulation of an ideal fluid flow must remain constant, because the viscosity term that could force the fluid to spin is negligibly small. The sum of the wake vorticity is exactly equal to the negative of the bound vorticity of the foil.

A foil accelerated instantaneously from rest will therefore not generate a full circulation immediately, since the vortices in the wake also help mitigate the infinite velocity at the trailing edge. The lift from a such a foil is called the Wagner Function [37], as illustrated in Fig 2-2. Wagner theory predicts that a step change in foil velocity will initially have only half of its steady lift value.

Theodorsen's flutter theory [32] extends Wagner's result by determining the lift

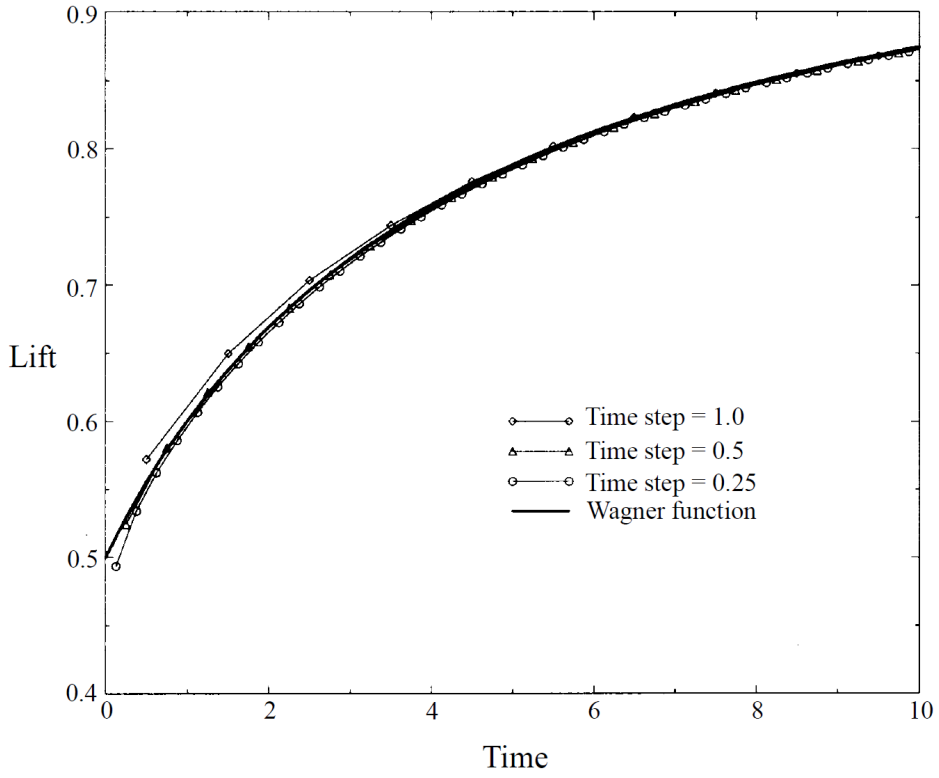

Figure 2-2: *Wagner Function* - A flat plate impulsively started at velocity U will create a starting vortex that affects the instantaneous lift. The above figure illustrates the ratio between the instantaneous lift and steady state lift, as a function of chord lengths of travel. Taken from Anderson et al. [1]

on a foil that is both sinusoidally heaving h and pitching θ, assuming small amplitude for each, by approximating the foil wake as a line of point vortices. The Theodorsen theory accounts for the constantly varying circulation of both the foil and the wake.

Theodorsen's model [32] consists of three parts: the quasi-steady lift L_{qs}, the added mass lift L_{am}, and the Theodorsen transfer function $C(s)$ to account for wake-induced lift:

$$L = L_{qs}C(s) + L_{am} \tag{2.9}$$

The quasi-steady lift is the lift predicted by the Kutta Condition without a wake. The quasi-steady lift for a foil rotated about quarter-chord is given by:

$$L_{qs} = \rho \pi c U (U\theta - \dot{h} + \frac{1}{2} c\dot{\theta}) \tag{2.10}$$

Note that if the foil has no pitching velocity $\dot{\theta}$, then the quasi-steady lift is proportional to the instantaneous angle of attack:

$$\alpha = \theta - \text{atan}\left(\frac{\dot{h}}{U}\right) \approx \theta - \dot{h}/U \tag{2.11}$$

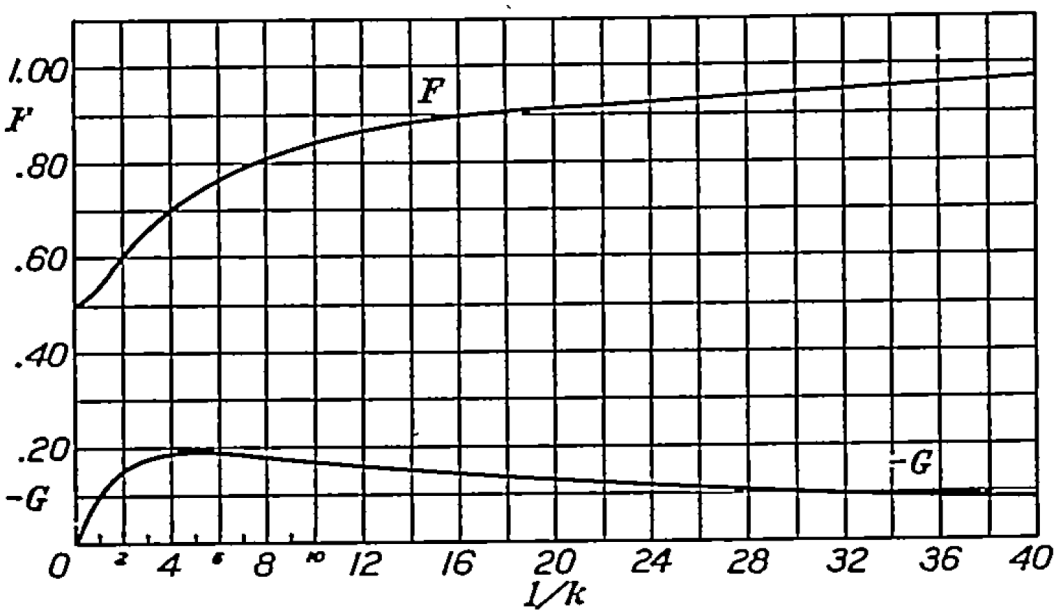

Figure 2-3: *Theodorsen Transfer Function* - An oscillating foil of small amplitude will have its lift the output of a transfer function $C(k) = F(k) + iG(k)$, where the input is the quasi-steady lift. Note that at low and high frequencies, the phase is zero. Taken from Theodorsen [32].

The wake effects are captured by the transfer function $C(s)$ (Fig. 2-3), which is normally expressed in terms of Bessel Functions. Numerous historical approximations exist, nicely enumerated by Brunton and Rowley [3].

The lift due to added mass is proportional to the acceleration of the foil, given by:

$$L_{am} = \frac{1}{4}\rho c^2 (U\pi\dot{\theta} - \pi\ddot{h} + \frac{1}{4}\pi c\ddot{\theta}) \tag{2.12}$$

Theodorsen uses this unsteady lift formulation to predict when airplane wings

would exhibit aeroelastic flutter, caused by a vibrational coupling between the elasticity in the wing structure and the vortices in the wake. His formulation, however, has since been adapted into research on powered flapping flight [2, 20, 14, 8].

2.4 Delayed Stall Effects

The ideal potential flow theory only remains valid at low angles of attack; once a foil passes an angle of attack of roughly 15°, the flow separates from the upper surface of the foil, causing a loss of lift.

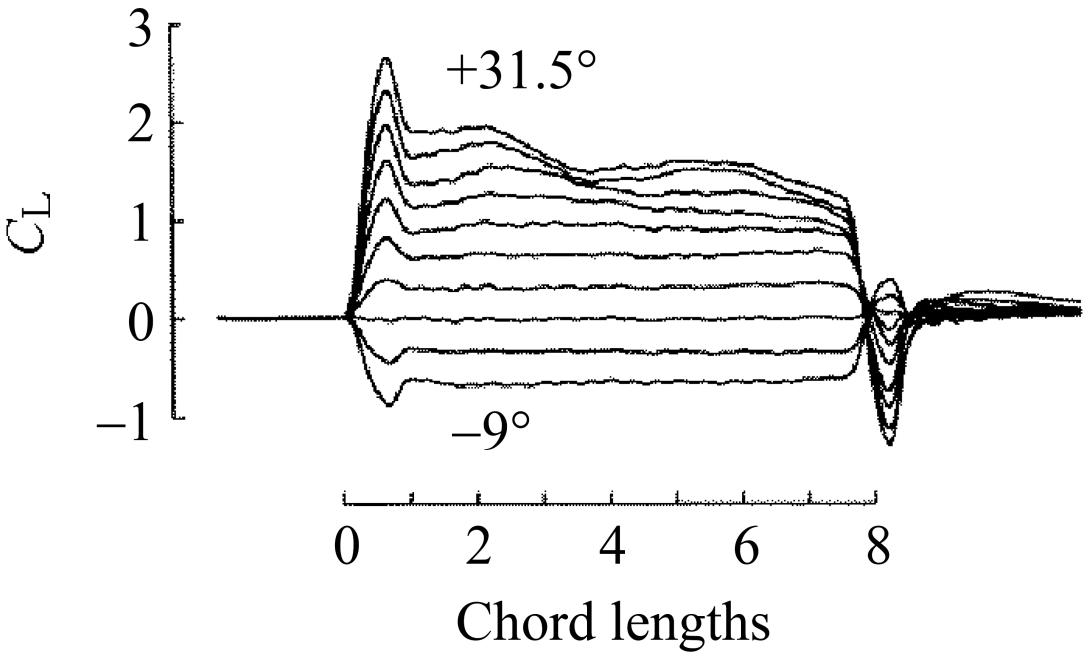

Figure 2-4: *Delayed Stall* - Numerous lift transients exist as a foil is impulsively started beyond its stall angle. The initial and final peaks indicate the added-mass forces from the foil accelerating, while the slow lift decay at higher angles of attack indicate the delayed stall. Taken from Dickinson and Gotz [5], at $Re = 192$ with 4.5° steps.

However, if a foil is rapidly moved beyond its stall angle and returned, the flow does not fully stall (Fig. 2-4) [1, 18, 5]. Stall is the steady-state phenomenon, while several transient flow structures exist as the stall develops. Many biological examples of flapping flight take advantage of this effect, often using large α without loss of lift.

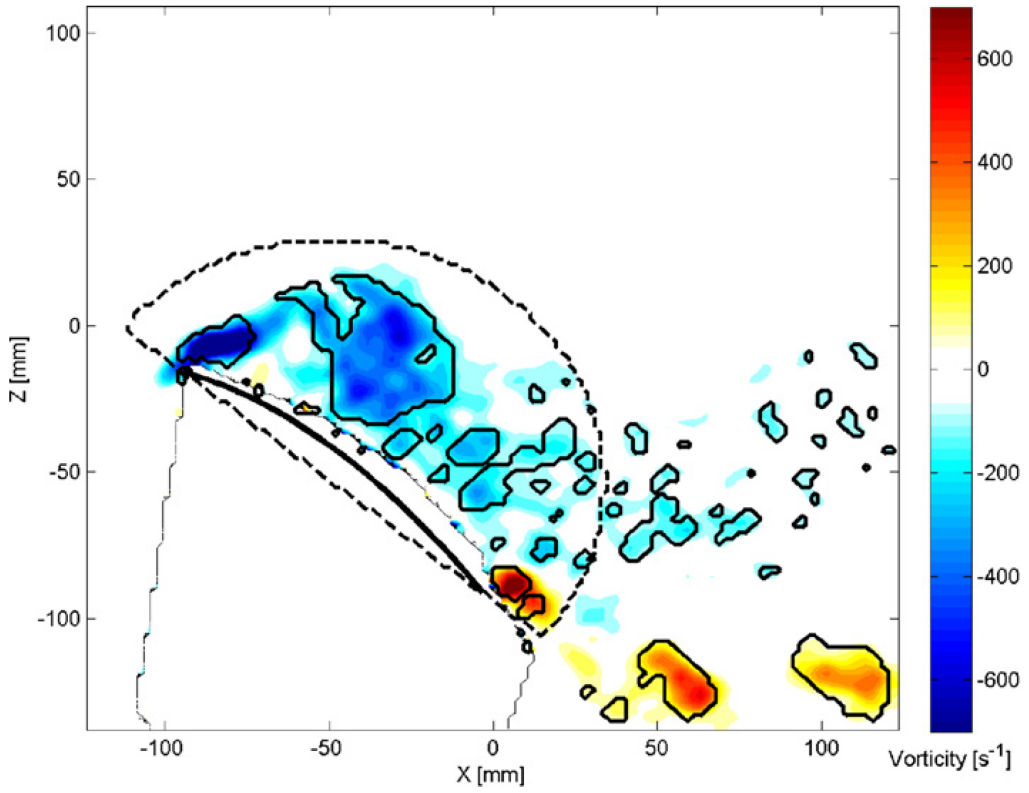

Figure 2-5: *Leading Edge Vortex* - A leading edge vortex (LEV) forming above a bio-inspired mechanical batoid wing. Taken from Koekkoek et al. [13].

The leading-edge vortex (LEV) is one example of a stall transient that can boost the lift (Fig. 2-5). As a foil passes the stall angle, the flow above the leading edge of the foil forms a vortex that acts as a low-pressure region, whose suction boosts the instantaneous lift. Leading edge vortices generally shed into the wake and a full stall develops, but stabilizing these beneficial structures is an active research field.

2.5 Flapping Foil Theory

A body experiencing drag will create a region of separated flow, and the shear layer on the border of this separated flow will form a regular pattern of vortices [26]. The vortex pattern has a remarkable consistency across the laminar flow regime, characterized by the Strouhal number:

$$St = \frac{fd}{U} \approx 0.2 \tag{2.13}$$

Where d is the width of the wake, f is the frequency of vortex shedding, and U is the free stream velocity. This wake is called the classic von Kármán vortex street. The von Kármán vortex street also exists in turbulent flows, only disappearing completely in the transition regime for very smooth bodies.

Remarkably, a flapping foil can also be used to generate thrust, demonstrated by Koochesfahani [14], through the creation of a *reverse* von Kármán vortex street. Figure 2-6 illustrates a wake taken from Koochesfahani [14], where the vortices appear staggered in the opposite orientation of the drag wake. This result is not predicted by Theodorsen [32], who limited his wake to a single line.

Using a flapping foil to generate thrust is inefficient unless it is also flapped at a Strouhal number around $0.2 - 0.4$ [36], illustrating another parallel with the drag wake. Efficiencies as high as 80% have been reported [1, 22] for such a flapping foil at these frequencies. Additionally, a wide range of animals have been observed taking advantage of the effect [25, 36]. Figure 2-7, taken from Taylor et al. [30] illustrates a number of animals across multiple phyla, all characterized by a small range of Strouhal frequencies.

Flapping foils, however, generate a large oscillating transverse force in addition to the thrust. This problem can be mitigated using in-line motion, where the foil is oscillated parallel to the free stream in addition to transverse. Licht et al. [15] notes that a reduction in the transverse force can be obtained without compromising the thrust efficiency. In-line motion in the opposite direction can instead be used to augment the transverse force.

This thesis explores the use of in-line motion on a flapping foil to improve the force performance, so that the flapping foil could be used as a maneuverable actuator on an autonomous vehicle.

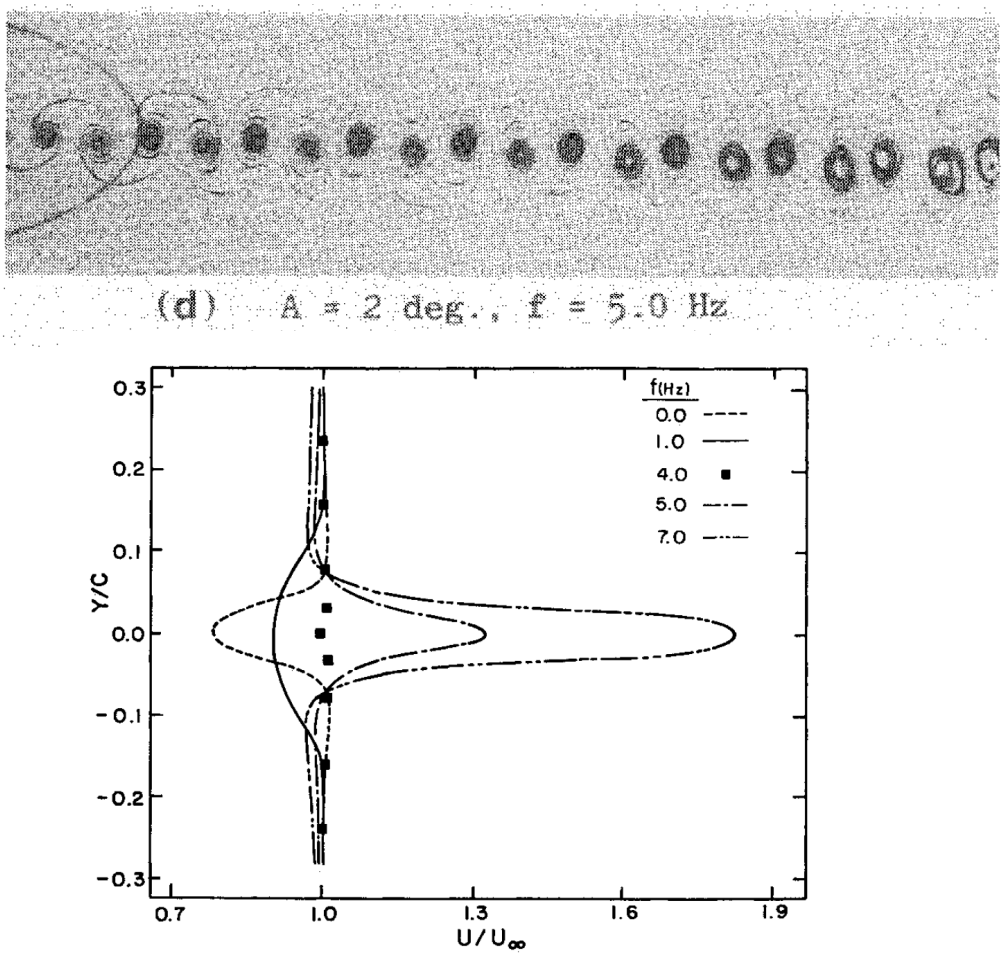

Figure 2-6: *Thrust-Producing Reverse von Kármán Wake* - The wake of an oscillating foil will generate a reverse von Kármán vortex wake. **Top:** The reverse von Kármán wake consists of a vortex street of staggered vortices. **Bottom:** The mean flow one chord-length behind the foil, indicating a thrust wake. Taken from Koochesfahani [14], chord $Re = 12,000$ NACA0012 oscillated with 2° amplitude about quarter-chord.

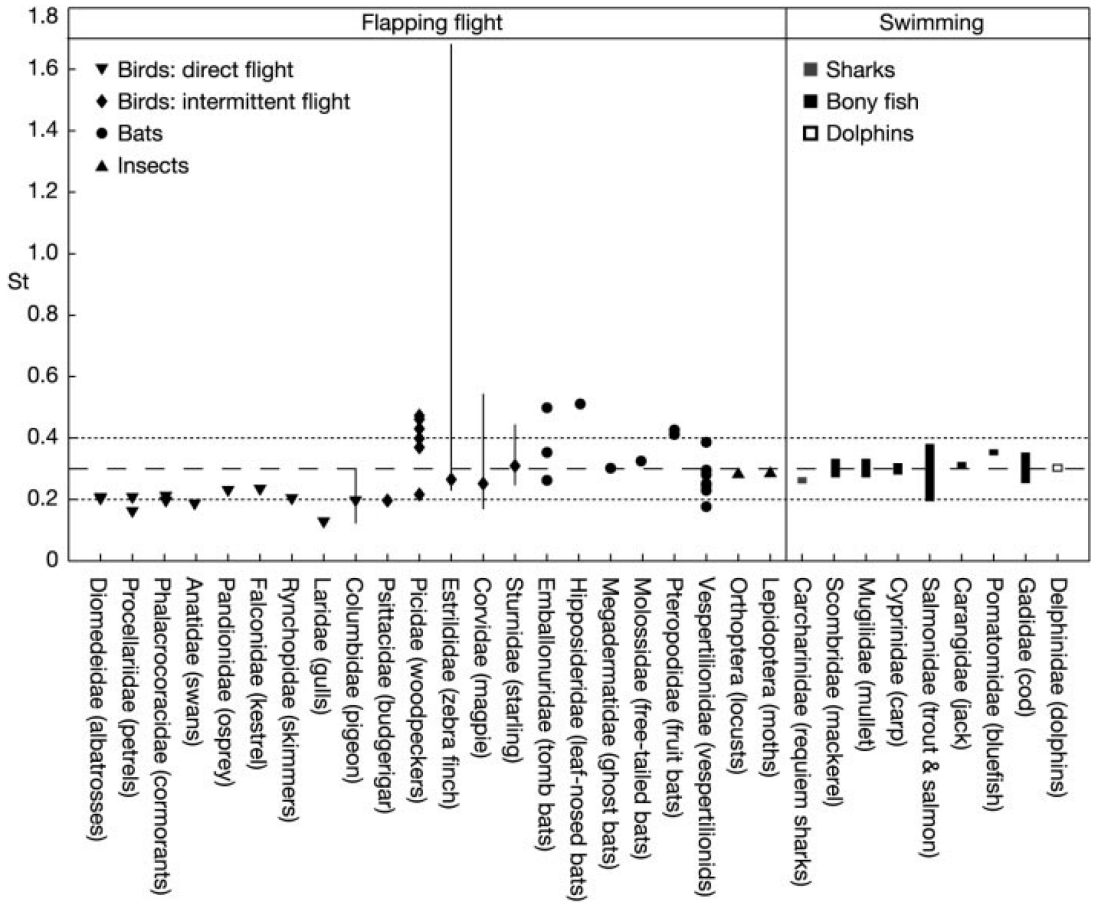

Figure 2-7: *Animals Flapping at Narrow Band of Strouhal Frequencies* - A wide range of animals across multiple phyla and fluids flap at a narrow band of Strouhal numbers, usually residing between $St = 0.2$ and $St = 0.4$. Taken from Taylor et al. [30].

Chapter 3

Materials and Methods

We conducted a series of tests on a high aspect ratio foil in order to explore the parametric range of an added in-line motion, combined with a power downstroke and a feathering upstroke.

3.1 Experimental Apparatus

We test a series of flapping trajectories on foils in a glass tank, 2.4m by 0.75m by 0.75m, located in the MIT Towing Tank Facility. The towing apparatus is equipped with four actuators for controlling the motion of the foil (Fig. 3-1):

1. A main carriage motor that tows the entire assembly at a constant speed U, through a chain drive mechanism that is tensioned by a pull-cord linear velocity transducer.

2. A Parker Trilogy linear servomotor capable of moving the foil transverse to the flow, $y(t)$.

3. A second Parker Trilogy linear servomotor that moves the foil in-line with the flow, $x(t)$, adding a time-varying velocity to the constant speed U.

4. A rotary Yaskawa Sigma Mini Servomotor that actuates the foil pitch motion $\theta(t)$.

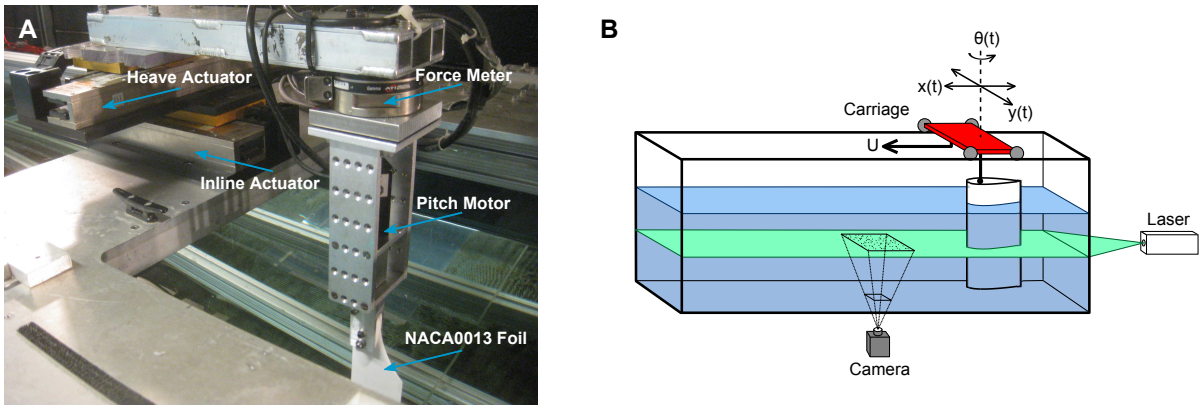

Figure 3-1: *Towing Tank Schematic* - **A:** Photograph of the towing tank apparatus. The foil is attached to a pitch motor, which is mounted to the force meter. The entire assembly is then mounted on an two-axis linear stage. **B:** The motion system rests on a carriage that moves down the tank at velocity U.

The x, y, and θ motors are controlled through a Delta Tau PMAC2A-PC motion controller, amplified by two Copley Controls XENUS Digital Drives and a Yaskawa Sigma Mini motor controllers respectively. The forces are measured with an ATI Gamma force transducer, logged through a LabVIEW interface. All data processing is performed in MATLAB. The foil is a lightweight NACA0013 carbon fiber blade, with a true chord length of 55 mm and aspect ratio of 6.5. The trailing edge of this foil is not perfectly sharp (0.6 mm width) due to manufacturing limitations, cutting approximately 3% off the ideal chord length. All data is filtered with a 5th order low-pass Butterworth filter at 10 Hz to remove electrical and vibration effects without affecting the highest frequency fluid forces - usually the 6 Hz Strouhal shedding caused by the foil thickness.

The tank includes a movable false bottom, which was raised to within 8 mm of the foil tip, or 15% of the chord. The false bottom reduces the effect of the tip vortex [28], which in addition to the free surface, allows us to approximate the fluid dynamics as a 2D unsteady foil problem. Therefore, while the nominal foil aspect ratio is 6.5, the effective aspect ratio is larger. Wave-making effects in previous experiments were found to be negligible at the carriage speed used, 0.2 m/s.

We visualize the foil wake using planar Particle Image Velocimetry (PIV), illuminated by a Quantronix Darwin Nd:YLF laser (527 nm wavelength) located behind

the foil. The laser is collimated and then expanded into a 4 mm thick plane, while the tank is seeded with 50 micron polyamid particles. A 10 bit Imager Pro HS CMOS high-speed camera, located below the tank facing upwards, records the flow at 600 Hz with 949x749 pixels. All PIV time-series processing is performed in DaVis 7.2 using the following parameters:

- Three-frame gap to allow adequate seed motion
- A 5 pixel sliding background preprocessing to remove unwanted reflections
- Three interrogation window passes, first at 64 pixel and two at 32 pixels with 50% overlap
- A post-processing vector median filter and a 3x3 smoothing filter

An optical limit switch is located about a meter down the tank, which both triggers the PIV system and indexes the PIV dataset to the LabVIEW data log. Final data processing is performed in MATLAB, using the PIVMat toolbox to import the data.

3.2 Parametrization of the flapping motion

The foil is towed along the tank at constant speed U and is allowed to move in three degrees of freedom:

1. motion transversely to the direction of towing, or heave $y(t)$;
2. angular motion about a spanwise axis, or pitch $\theta(t)$; and
3. motion parallel to the direction of towing, or surge $x(t)$.

The surge and heave motions, $x(t)$ and $y(t)$, are set to be sinusoidal motions with the same frequency of oscillation. Their relative phase is set equal to zero, which is only an approximation of the observed animal motion, resulting in the foil translating back and forth along a straight line when viewed in the carriage's reference frame. We call this line the stroke line (Fig. 3-2), defined by an angle β with respect to the

horizontal. The stroke line is the 2D analog to the stroke plane, a simplification used in several biological studies of flapping animals [33, 16, 34, 29].

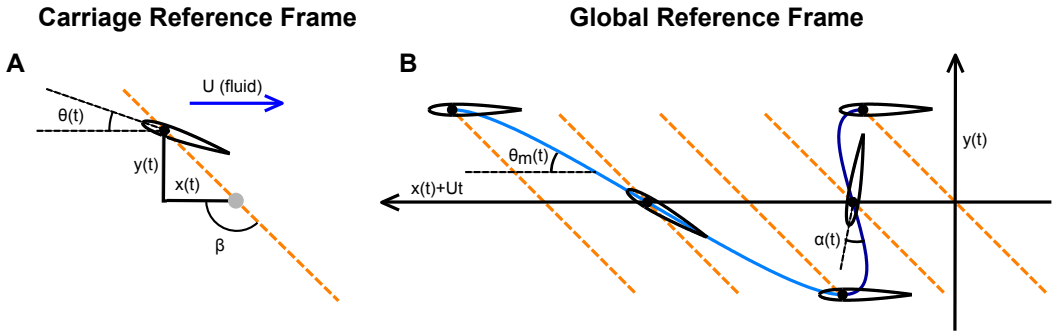

Figure 3-2: *Definition of variables* - **A:** In the carriage reference frame, the foil travels along a single stroke line (illustrated in orange) with sinusoidal components as function of time. This line is defined by the angle β with respect to the horizontal. **B:** As the carriage moves at constant velocity U, the stroke line translates, resulting in a skewed-harmonic trajectory for the foil. Ignoring the induced velocities from the wake vortical patterns, the nominal angle of attack α is the angle between the foil pitch θ and the angle of foil motion θ_m.

The motions in x and y are therefore given by the expressions:

$$y(t) = h\,\cos(2\pi f t) \tag{3.1}$$

$$x(t) = \frac{h}{\tan(\beta)}\,\cos(2\pi f t) \tag{3.2}$$

where h is the amplitude of the transverse motion, β is the stroke angle, and f is the flapping frequency (in Hz). Note that the above parametrization keeps the total transverse displacement at $2h$, independent of β. By assuming that the wake width is the same as the transverse displacement, we can thereby define a Strouhal number [36]:

$$St = \frac{2fh}{U} \tag{3.3}$$

For symmetric flapping foil propulsion, high efficiency thrust production occurs in wakes with a Strouhal number in the range of $0.2 < St < 0.4$, which also accurately predicts the flapping frequencies of various birds and swimming creatures [30, 19, 35].

The angle of foil motion θ_m is dependent on the velocity of the foil in the global reference frame:

$$\theta_m(t) = \text{atan}\left(\frac{\dot{y}(t)}{\dot{x}(t) + U}\right) \tag{3.4}$$

The angle of the incoming flow relative velocity, θ_f, is influenced by the kinematics of the foil as well as the induced velocities from the vortical structures in the wake. For simplicity, we approximate θ_f with θ_m. The approximate angle of attack is, therefore:

$$\alpha(t) = \theta(t) - \theta_m = \theta(t) - \text{atan}\left(\frac{\dot{y}(t)}{\dot{x}(t) + U}\right) \tag{3.5}$$

Following Hover et al. [10], we impose the functional form of the angle of attack, rather than that for the pitching motion. This was found to be significant for symmetrically flapping foils at high Strouhal numbers, when a sinusoidal pitch motion causes multiple peaks in the angle of attack and degradation of performance [10]. It should be noted that an asymmetric flapping profile, where $\beta \neq 90°$, will not create a symmetric wake. We therefore set the intended angle of attack $\alpha(t)$ directly, discussed in detail in Section 4, then derive the required $\theta(t)$ from the known $\theta_m(t)$.

$$\theta(t) = \alpha(t) + \text{atan}\left(\frac{\dot{y}(t)}{\dot{x}(t) + U}\right) \tag{3.6}$$

Using Eqns 3.1, 3.2 and 3.6, we parametrize the flapping trajectory first by setting the shape of $\alpha(t)$, and employing four dimensionless parameters (Strouhal number St, stroke angle β, heave to chord ratio h/c, and chord Reynolds number $Re = Uc/\nu$). We further limit these parameters to the following ranges that fit our experimental apparatus:

$$\begin{gathered} 0.1 < St < 0.5 \\ 45° < \beta < 135° \\ h/c = 1 \\ Re = 11,000 \end{gathered} \tag{3.7}$$

The constant heave to chord ratio is in accordance with the values that have been used in high efficiency foils [1], but it is only representative of animal motion, expecially for 3D flapping birds; however, this assumption keeps the parameter set small enough to focus on the in-line motion effects. Our chosen experimental Strouhal range overlaps with the expected high-efficiency and high-thrust flaps investigated in Anderson et al. [1], while the stroke angle β is limited by the travel of the X motion actuator. The Reynolds number of 11,000 was chosen to both fit the intended regime for biological propulsion and to integrate easily into our existing tank equipment.

3.3 Performance Metrics

We record the forces and define metrics for force production which can serve for parametric optimization.

3.3.1 Foil Forcing

In each experiment, we recorded the following forces and moments on the foil as function of time:

$$\mathbf{F}(t) = \begin{bmatrix} F_x(t) \\ F_y(t) \\ M_\theta(t) \end{bmatrix} \tag{3.8}$$

Where F_y is the transverse force, F_x is the thrust force, and M_θ is the torque about the rotation axis, after correcting for acceleration of the reference frame. We non-dimensionalize these forces using the dynamic pressure and reference (one-sided) foil area to find the following transverse and thrust force coefficients:

$$C_x(t) = \frac{F_x(t)}{0.5\rho U^2 S} \quad C_y(t) = \frac{F_y(t)}{0.5\rho U^2 S} \tag{3.9}$$

$$C_m(t) = \frac{M_\theta(t)}{0.5\rho U^2 S c} \tag{3.10}$$

Where S is the projected area of the foil (one-sided), viz. the span b times the chord c.

3.3.2 Propulsive Efficiency

We compute the propulsive efficiency as the ratio of output power P_{out} to input P_{exp} power, i.e. the product of average thrust times forward speed, divided by the average expended power:

$$\begin{aligned} P_{out}(t) &= \tfrac{1}{T}\int_0^T F_x(t)U\,dt \\ P_{expended}(t) &= \tfrac{1}{T}\int_0^T [F_x(t)\dot{x}(t) + F_y(t)\dot{y}(t) + M_z(t)\dot{\theta}(t)]dt) \end{aligned} \tag{3.11}$$

$$\eta = \frac{P_{out}}{P_{exp}} \tag{3.12}$$

Previous experiments in Licht et al. [15] have shown that downstream in-line motion can increase the propulsive efficiency of the flapping foil in the range $0.2 < St < 0.4$, with minor reduction in thrust.

3.3.3 Force Quality: Effectiveness of Controlling Force Direction

A principal reason for using in-line motion is to achieve better force control, in the sense of directing the force as desired and minimizing any components in the perpendicular plane. This is in principle particularly difficult in a flapping foil which is subject to large oscillatory forces.

Hence we define a metric of force quality as the magnitude of the parasitic force which is perpendicular to the desired direction, expressed as the root-mean-square of the undesirable force over the mean value of the total force. For example, in the case of a symmetric thrust-producing flap, the desired force is in the $\hat{\mathbf{x}}$ direction. Therefore, we want to minimize the oscillation in F_y.

The following definition covers a wider range of flapping profiles: Restricting the derivation to two dimensions, we express the instantaneous force into a reference

frame consisting of the direction of intended force, expressed through the unit vector $\hat{\mathbf{n}}_i$, and the perpendicular direction. Ideally the flapping actuator would produce a force only in the direction of $\hat{\mathbf{n}}_i$, and hence no force in the perpendicular direction.

$$\hat{\mathbf{n}}_i = \begin{bmatrix} \hat{a}_1 \\ \hat{a}_2 \end{bmatrix} \tag{3.13}$$

$$\begin{bmatrix} F_{\parallel}(t) \\ F_{\perp}(t) \end{bmatrix} = \begin{bmatrix} \hat{a}_1 & \hat{a}_2 \\ -\hat{a}_2 & \hat{a}_1 \end{bmatrix} \begin{bmatrix} F_x(t) \\ F_y(t) \end{bmatrix} \tag{3.14}$$

Where $F_{\parallel}(t)$ is the instantaneous force parallel $\hat{\mathbf{n}}_i$, and $F_{\perp}(t)$ is the instantaneous force perpendicular to $\hat{\mathbf{n}}_i$. We quantitatively judge the cleanliness of the flapping profile by the root mean square of $F_{\perp}(t)$, which we then normalize by the mean force:

$$RMS(F_{\perp}) = \sqrt{\frac{1}{T}\int_0^T F_{\perp}(t)^2 dt} \tag{3.15}$$

$$\sigma^* = \frac{RMS(F_{\perp})}{\|\mathbf{F}_{mean}\|} \tag{3.16}$$

The non-dimensional metric σ^*, therefore, measures the amount of unintended force oscillation relative to the main intended force.

Chapter 4

Experimental Results

This chapter discusses the force performance of Trajectories I, II, and III from Table 1.1. The PIV wake visualization for these trajectories is given in the appendix.

4.1 Trajectory I - Symmetric Flapping Profile

As a basis for comparison, setting the stroke angle at $\beta = 90°$ results in a classic symmetric flap similar to those studied extensively theoretically and experimentally [32, 27, 36, 10, 1]; we impose a sinusoidal variation for the angle of attack α rather than for the pitching angle θ.

$$\alpha(t) = \alpha_{max} \sin(2\pi f t) \tag{4.1}$$

$$\theta(t) = \alpha(t) + \text{atan}\left(\frac{\dot{y}(t)}{\dot{x}(t) + U}\right) \tag{4.2}$$

For this profile, we set $\alpha_{max} = 25°$. While $25°$ is higher than the recorded stall angle for a NACA0013 under steady towing conditions, unsteady foils can maintain lift at high angles of attack because of delayed stall effects [1, 18].

Results for this symmetric flap are given in Fig. 4-1, averaged over 5 trials of 2 cycles each. Note that the thrust coefficient C_x has two peaks, caused by the positive and negative lift on the downstroke and upstroke. Also note that there is substantial

force perpendicular to the mean force direction - all the transverse force C_y integrates to zero but would oscillate a vehicle driven by the foil during the flap. In this example, the non-dimensional oscillation cost $\sigma^* = 3.1$, so C_y has an RMS of 3.1 times the mean of C_x. As we show below, flaps that use in-line motion can be designed to have far smaller oscillation costs.

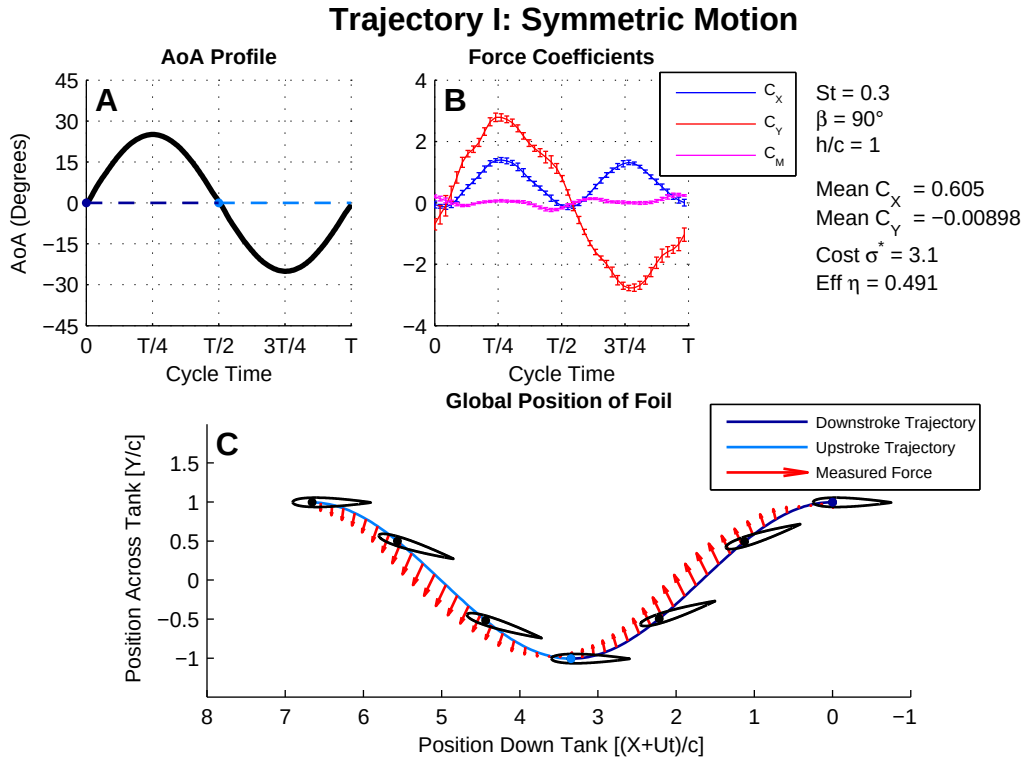

Figure 4-1: *Trajectory I: Symmetric Flap* - Experimental data for flapping perpendicular to the mean flow ($\beta = 90°$), at frequency given by $St = 0.3$. **A:** The angle of attack, ignoring the wake-induced velocity, achieved by the θ motor. **B:** The instantaneous force coefficients in the in-line and transverse directions (X and Y), normalized by $\frac{1}{2}\rho SU^2$. All error bars refer to one standard deviation over 5 runs of 3 flaps per run, while ignoring the first cycle in each run. **Right:** The different parameters used to define the motion trajectory, along with the force performance of the flap. **C:** The force superimposed on the foil trajectory in the global frame. Foils are plotted every $\frac{1}{6}$ of a flapping cycle.

4.2 Trajectory II - Forward Moving Downstroke to Augment Transverse Force

Setting the stroke angle $45° < \beta < 90°$ results in a dramatic increase in the transverse force C_y during the downstroke, largely clean of unwanted force oscillation. Fig. 4-2 illustrates an example profile at $St = 0.3$ and $\beta = 45°$. There are many ways to define $\alpha(t)$ profiles over the course of the flapping motion, which can have a strong effect on the resultant force [10]. For this example, we chose a single peaking profile for the downstroke. To effect a smooth transition between downstroke and upstroke, we use an offset cosine wave that blends well at the boundaries, defined by a single additional parameter α_{max}, which can be seen graphically in Fig. 4-2:

$$\alpha(t) = \begin{array}{ll} \alpha_{max}(0.5 - 0.5\cos(4\pi f t)) & t \mod T \leqq T/2 \\ 0 & t \mod T > T/2 \end{array} \tag{4.3}$$

Where T is the flapping period, and $\alpha_{max} = 25°$ is the angle of attack at the middle of the downstroke.

As a general observation, forward moving flaps during the downstroke exhibiting good performance are easy to design and set up. The large downstroke lift, largely isolated in one direction in the global frame, removes the unwanted force oscillation present in a symmetric flap (in this example $\sigma^* = 0.28$). Note that there are small maxima and minima in the lift (Fig. 4-2) at the beginning and end of the upstroke when the foil rotates quickly; however, these are far smaller than the large values of the downstroke lift.

The fact that lift is largely restricted to the downstroke for this specific motion trajectory is heavily supported by 2D unsteady foil theory. According to this theory, the lift per unit span is dependent on three components: the quasi-steady lift, the added mass, and wake effects. If for the moment we focus only on the quasi-steady term, derived for a foil rotated at quarter-chord [32]:

$$L_{qs}(t) = \frac{1}{2}\rho c v(t)\, 2\pi[v(t)\alpha(t) + \frac{c}{2}\dot{\theta}(t)] \tag{4.4}$$

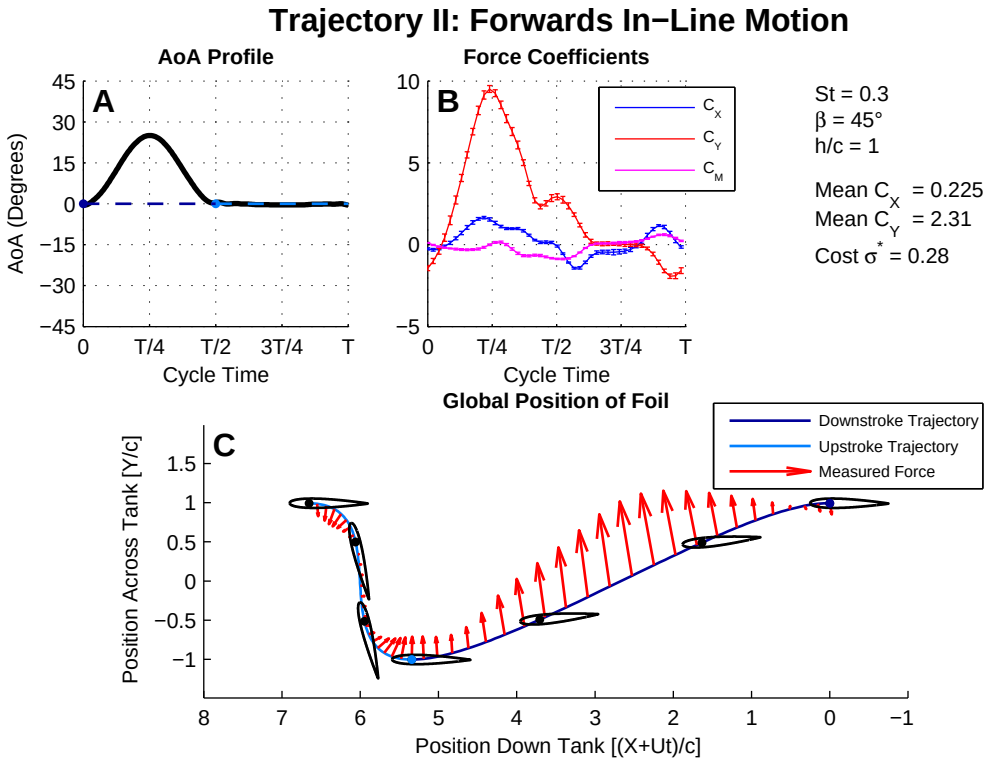

Figure 4-2: *Trajectory II: Bird-Like Forward Biased Flap* - Experimental data for flapping forward during the downstroke, along an angle of $\beta = 45°$, with flapping frequency given by $St = 0.3$. Descriptions of the subplots are same as in Fig. 4-1. Note that lift production is almost entirely restricted to the downstroke; furthermore, the increased lift production boosts the transverse force C_y with little unwanted force oscillation in the thrust C_x. This good force production performance was achieved with a very simple motion definition, a partial cosinusoidal $\alpha(t)$ and sinusoidal heave and in-line motion along a 45° angle.

Where c is the chord and $v(t)$ is absolute velocity in the global frame:

$$v(t) = \sqrt{\dot{y}(t)^2 + (U + \dot{x}(t))^2} \tag{4.5}$$

And $\dot{x}(t)$ and $\dot{y}(t)$ are given by the derivatives of Eqns 3.1 & 3.2:

$$\dot{x}(t) = -\frac{2\pi f h}{\tan\beta}\sin(2\pi f t) \qquad \dot{y}(t) = -2\pi f h \sin(2\pi f t) \tag{4.6}$$

During the downstroke, $v(t)$ is larger than during the upstroke, since $\beta < 90°$ causes $\dot{x}(t)$ to be positive when $\sin(2\pi f t)$ is positive. In other words, in a bird-like

flap, the foil is moving substantially upstream during the downstroke, meaning that the relative velocity of the foil is much higher. This can be verified visually in Fig. 4-2C: the foils shown on top of the global motion trajectory are at constant time increments, illustrating the faster velocity during the downstroke.

Returning to Eqn 4.4, the quasi-steady lift is dominated by the angle of attack term $v(t)\alpha(t)$ during the downstroke, but $\alpha = 0$ during the upstroke, making the other term $\frac{c}{2}\dot{\theta}(t)$ dominant during the upstroke. However, since $\pi\rho S v(t)$ is much smaller on the upstroke than on the downstroke, we have little quasi-steady lift on the upstroke compared to the downstroke. In effect, the foil is moving fastest when the largest forces are desired.

The unsteady lift due to wake effects and added mass additionally affect the total lift. However, they are generally small compared to L_{qs} and also scale with the velocity of the foil $v(t)$, meaning they are dwarfed by the quasi-steady lift during the downstroke. As a result, the lift is largely isolated to the downstroke, as supported by the experiment.

4.3 Trajectory III - Backwards Moving Downstroke to Augment Thrust Force

Setting the stroke angle $90° < \beta < 135°$ results in a thrust-producing flap, but the unsteady effects are far more pronounced. Fig. 4-3 shows the analogous flap to the previous example, with $St = 0.3$, $\beta = 135°$, and $\alpha(t)$ is the same as in Eqn 4.3. Since the intended force direction for this flap is horizontal thrust, the transverse forcing at the beginning and end of the upstroke caused by the rapid foil rotation is undesirable, drastically increasing σ^*. Additionally, the large negative thrust on the upstroke negates the effectiveness of the downstroke, caused by "memory effects" in the wake, viz. induced velocities from shed vorticity in the wake. Previous experiments in Licht et al. [15] show similar peaks indicating strong wake memory effects during the upstroke.

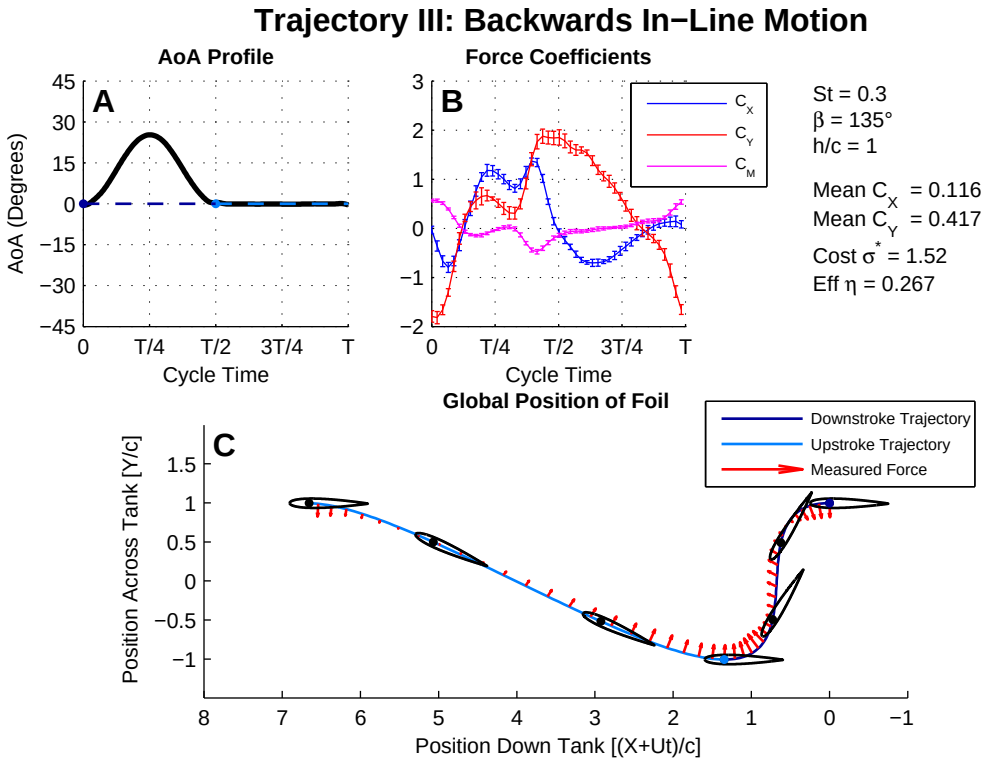

Figure 4-3: *Trajectory III: Turtle-Like Backwards Moving Downstroke* - Experimental data for a backwards moving downstroke, along an angle of $\beta = 135°$, at frequency given by $St = 0.3$. Descriptions of the subplots are same as in Fig. 4-1. Note that unlike the bird-like flap, this flap is intended to create thrust C_x, not transverse force C_y. Accordingly, the large transverse forces at the beginning and end of the downstroke are unwanted, as is the negative thrust during the upstroke.

The poor performance of this flapping mode can again be explained by analyzing $v(t)$. Since $\beta > 90°$ instead, $v(t)$ is now smaller on the downstroke than on the upstroke, exactly opposite of what happens in the forward moving downstroke. Effectively, the foil is *moving at its slowest when the intended force is highest*, making this type of motion trajectory far more difficult to effectively design. The quasi-steady lift during the slow downstroke is now closer in magnitude to unsteady effects throughout the rest of the flap.

Therefore, designing flaps that take advantage of backwards in-line motion is far more difficult, and significant correction is required to mitigate unsteady fluid dynamics.

Chapter 5

CFD Simulated Control Solution

Given the poor performance of Trajectory III (described in detail in Section 4.3), we introduce a control-based approach to mitigate the unwanted lift. This controller tests the following hypothesis: the unwanted forces that are difficult to exactly predict can be measured and subsequently counteracted in real-time using easily-predicted lift forces.

The intent of this control is therefore to create a force-profile follower, where the angle of attack of the foil is varied to create the intended force at the intended time during the flapping cycle.

Instead of implementing a real-time control solution on the experimental apparatus, we instead demonstrate its viability through a computational fluid dynamics (CFD) simulation. However, as is to be noted in the next chapter, an optimization-based solution is preferable, so this control scheme has yet to be implemented on the experimental apparatus.

5.1 CFD Methodology - Lilypad

The CFD codebase, described by Weymouth et al. [39], has been successfully used previously to investigate ship flows [39], cavity formation [38], and vanishing bodies [40]. As a brief description of the method, the simulation takes place on an evenly spaced cartesian grid that does not wrap to the body geometry. Instead, the nonlinear

fluid equations are integrated over the boundary using a kernel, defining a smooth interface between the body and the fluid.

The code therefore analytically combines the Navier-Stokes equations of the fluid velocity $\vec{u}$ with the body velocity $\vec{V}_{body}$ [38].

$$f_{body}(\vec{u}) = \vec{u} - \vec{V}_{body} \tag{5.1}$$

$$f_{fluid}(\vec{u}) = \frac{\partial \vec{u}}{\partial t} + (\vec{u} \cdot \vec{\nabla})\vec{u} + \frac{1}{\rho}\vec{\nabla}p - \nu\nabla^2\vec{u} \tag{5.2}$$

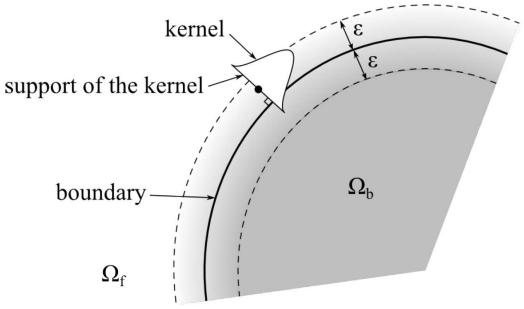

Figure 5-1: *CFD Solution Method* - The CFD solution consists of a static cartesian grid that does not wrap to the body boundary. Instead, the differential equations are integrated over a kernel on the body boundary, analytically combining the Navier-Stokes equations in of the fluid region Ω_f with the body boundary conditions of the body region Ω_b . Taken from [17].

An example flow field for our foil CFD simulation is shown in Figure 5-2, where the foil is oscillated between $\pm 5^\circ$ at $\omega = 2\pi$ radians per body length of travel. As expected by the model proposed by Theodorsen [32], a steady trail of vortices appear downstream of the foil, which summarily affects the lift. As a standard in all the simulations, the grid includes 64 gridpoints per foil chordlength and a NACA0012 foil.

For the purposes of this simulation, our intended chord Reynolds number is 11,000, in the regime typical of flapping foil actuators [1]. However, because of the discrete grid, the true effective Reynolds number is much lower, since the numerical solution has an additional diffusivity that acts similar to an augmented viscosity.

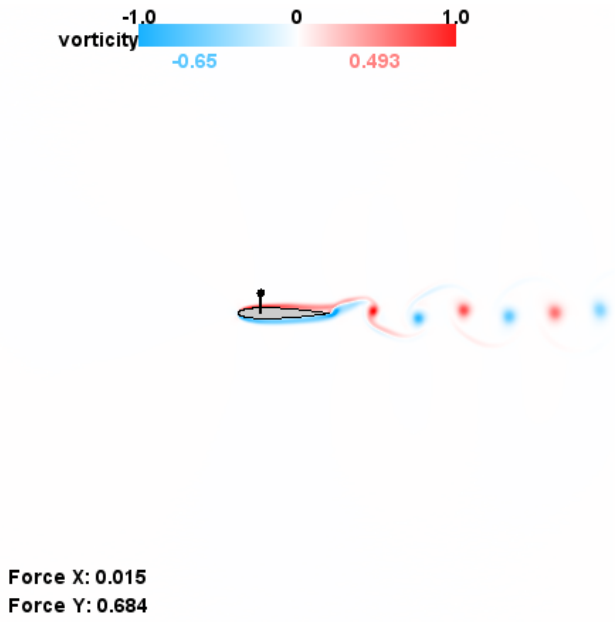

Figure 5-2: *Reverse von Kármán Vortex Street* - An example flow field from the CFD simulation, illustrating the classic reverse von Kármán vortex wake [14]. The color indicates the vorticity of the flow field, describing both the vortices shed into the wake and the vorticity in the boundary layer above and below the foil. The Force X and Force Y labels describe the instantaneous drag and lift respectively, and the black arrow illustrates the force vector.

5.2 Control Model

A simplified linear model of the lift output is necessary for developing the appropriate control law. We therefore look to the classic unsteady lift model of Theodorsen [32] as a starting point.

Theodorsen's model [32] consists of three parts: the quasi-steady lift L_{qs}, the added mass lift L_{am}, and the Theodorsen transfer function $C(s)$ to account for wake-induced lift:

$$L = L_{qs}C(s) + L_{am} \tag{5.3}$$

For our simple controller, we will use the quasi-steady assumption, approximating L with L_{qs}.

$$L \approx L_{qs}(t) = \frac{1}{2}\rho c v(t)\, 2\pi[v(t)\alpha(t) + \frac{c}{2}\dot{\theta}(t)] \tag{5.4}$$

Unfortunately, in the in-line motion flap, the global velocity of the foil v (Eqn 4.5) is time-varying, meaning that this lift model is not time-invariant. Additionally, given that the control input is some derivative of θ, then the angle of attack α includes the nonlinear added term θ_f from Eqn 3.4. However, if we normalize the output by $v(t)^2$ and subtract the known θ_f, then only one input term is non-LTI:

$$\alpha(t) = \theta(t) - \theta_f(t) \tag{5.5}$$

$$\frac{L_{qs}(t)}{v(t)^2} + \rho c\pi\theta_f(t) = \rho c\pi\theta(t) + \frac{\rho c^2\pi}{2v(t)}\dot{\theta}(t) \tag{5.6}$$

We can subsequently approximate the second term with $\frac{\rho c^2\pi}{2U}\dot{\theta}(t)$ and call the remainder a disturbance $d(t)$. Adding the added mass and wake effects into the disturbance as well, we achieve the following linear model:

$$y_{output} = \frac{L(t)}{v(t)^2} + \rho c\pi\theta_f(t) \approx \rho c\pi\theta(t) + \frac{\rho c^2\pi}{2U}\dot{\theta}(t) + d(t) \tag{5.7}$$

Replacing $a = \rho c\pi$ and $b = \frac{\rho c^2\pi}{2U}$, and setting the input $u = \dot{\theta}$ we achieve the following Laplace domain model:

$$y_{output} = \frac{a + bs}{s}u + d \tag{5.8}$$

Finally, we can develop the following pole-placement trajectory follower for y_{output}, using the error $e = y_{output} - y_{desired}$:

$$\tau\dot{e} + e = 0 \tag{5.9}$$

$$\tau[(a + bs)u - sy_{desired}] + y_{output} - y_{desired} = 0 \tag{5.10}$$

By integrating both sides, and ignoring initial conditions, we achieve a time-domain model in terms of the foil pitch $\theta = u/s$.

$$\tau(a\theta + b\dot{\theta} - y_{desired}) + \int y_{output} - y_{desired} dt = 0 \tag{5.11}$$

Discretizing and solving for the new θ_{N+1} and $\dot{\theta}_{N+1} = \frac{\theta_{N+1} - \theta_N}{\Delta t}$ each timestep:

$$\theta_{N+1} = \frac{y_{desired} + \theta_N \frac{b}{\Delta t} + \frac{1}{\tau} \sum y_{desired} - y_{output} \Delta t}{a + \frac{b}{\Delta t}} \tag{5.12}$$

This controller could clearly be improved in a number of ways, either by including integral error dynamics into Eqn 5.9 to mitigate a constant disturbance d, or by creating a truly time-varying control instead of LTI. However, the simple controller appropriately and stably rotates the foil to compensate for unwanted lift forces.

5.3 Trajectory IIIb - Closed-Loop Lift Control

The results of this closed-loop lift control can be found in Figure 5-3. The lift controller follows a partial cosinusoid lift trajectory, similar to Eqn 4.3, but includes an additional gain from steady foil theory:

$$L_{desired}(t) = \begin{array}{ll} \rho c v(t)^2 \pi \ \alpha_{max}(0.5 - 0.5\cos(4\pi f t)) & t \mod T \leqq T/2 \\ 0 & t \mod T > T/2 \end{array} \tag{5.13}$$

This desired lift function is the steady lift expected from the time-varying angle of attack of Trajectory III. The controller will therefore try to mitigate all the unsteady lift effects in Trajectory III, leaving only the wanted steady lift.

As indicated in Fig. 5-3, the controller successfully isolates the lift purely to the downstroke. The angle of attack function (Fig 5-3A) clearly shows the control scheme adding additional features to mitigate the unwanted downforce and upforce at the beginning and end of the downstroke, when the foil rotates the fastest. Additionally, the control removes most of the upstroke lift, with only small disturbances (Fig 5-3B).

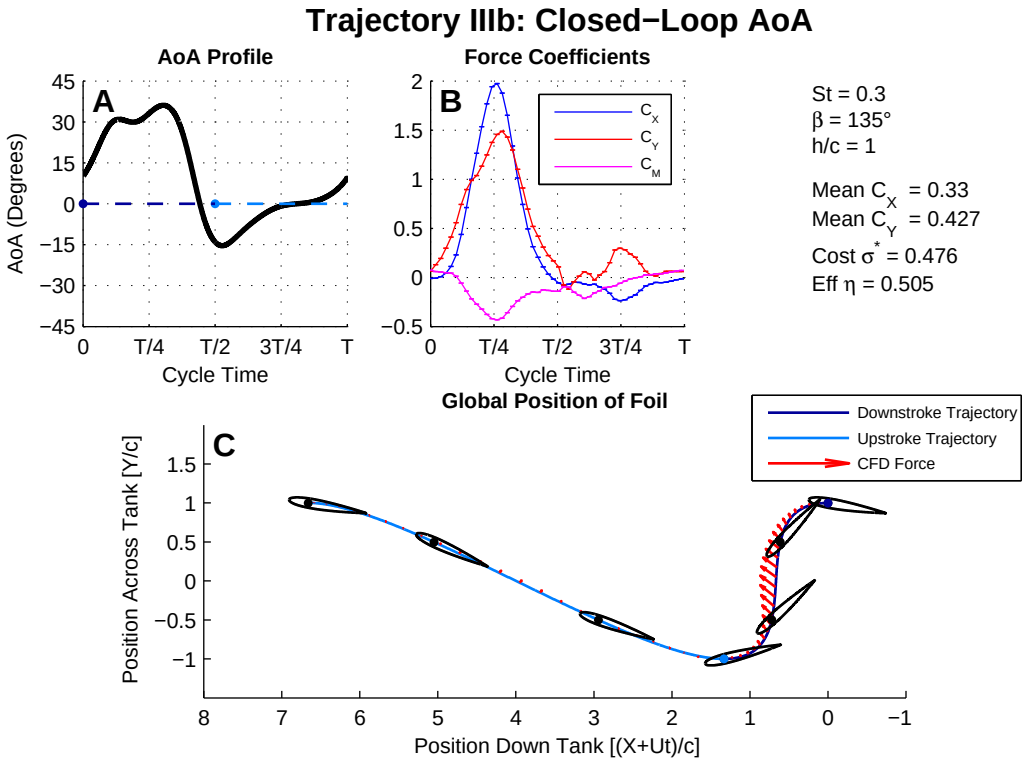

Figure 5-3: *Trajectory IIIb: Closed-Loop AoA* - CFD Force data for the control scheme, changing the foil AoA to follow a desired lift function. Similar to Trajectory III, this trajectory flaps along a stroke angle of $\beta = 135°$, at frequency given by $St = 0.3$. Descriptions of the subplots are same as in Fig. 4-1.

Figure 5-4 illustrates the flow state at the end of the downstroke, when the control algorithm is using a negative angle of attack to mitigate unwanted vertical force.

5.4 Lift Control Discussion

However, the force trajectory in Fig. 5-3 demonstrates a clear problem with using the control approach. While the lift is entirely isolated to the downstroke, the downstroke lift still causes substantial transverse force C_y, which may or may not be desired.

To have complete control over the force direction, the Strouhal St and stroke angle β must also be varied so that the downstroke lift is correctly oriented. Additionally, there is no compelling reason that the ideal lift trajectory should take the sinusoid form given in Eqn 5.13. The proper control algorithm would therefore be better suited

as an optimization problem, changing the all the trajectory parameters to minimize some defined cost function.

Most importantly, this control approach over-confines the problem by assuming that the solution must be performed in real-time, while the foil is in motion. However, the unwanted lift force originates mostly as unmodeled dynamics, not as a stochastic disturbance. Repeating the same motion trajectory will roughly reproduce the same unsteady lift forces.

A better solution is therefore to develop the trajectory parameters a-priori, perform an experimental or CFD trial, and then close the control loop *in between trials*. This type of feedback could design motion trajectories that mitigate unmodeled forces without the need for real-time control. A real-time controller may also be necessary to reject true flow disturbances, but it should be posed as a secondary problem about an optimized motion trajectory.

Chapter 6 develops this optimization routine, using a more advanced force model, while Chapter 7 illustrates three example motion trajectories designed using the technique. A real-time controller about these optimized trajectories has been reserved for future work.

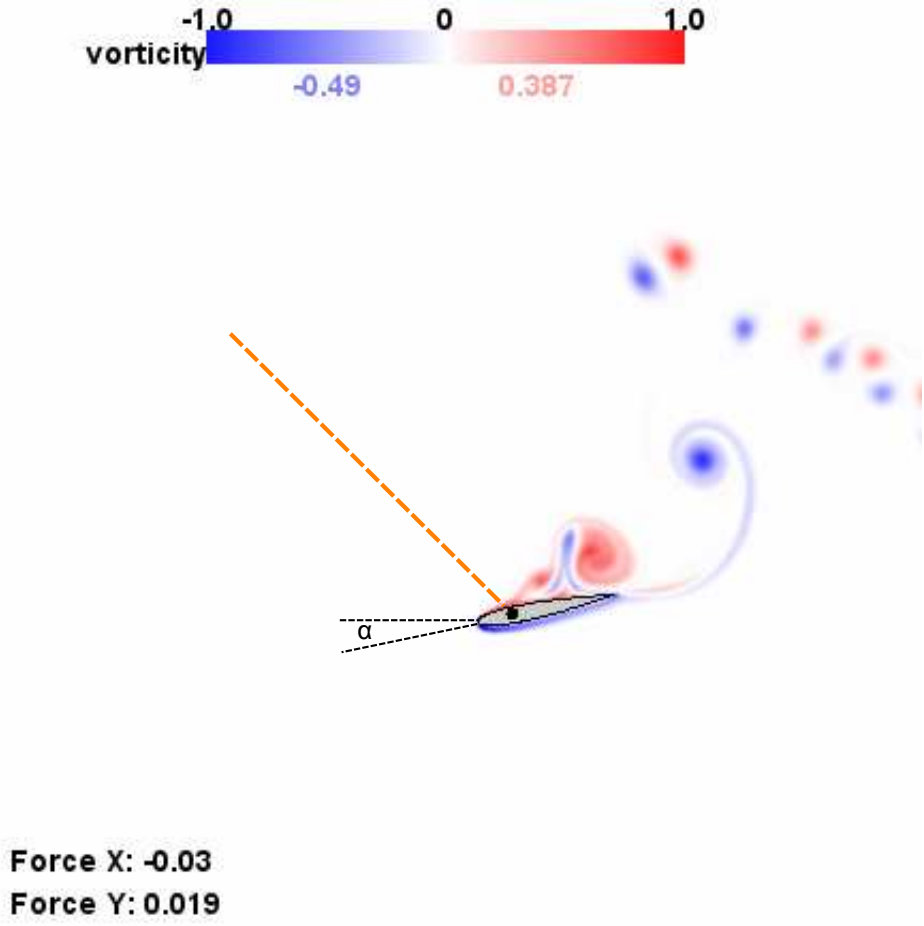

Figure 5-4: *CFD Flow Visualization on Trajectory IIIb* - The CFD simulation illustrates how the angle of attack can be varied to mitigate unwanted lift. The dashed orange line indicates the stroke angle, flow is traveling to the right. This image was taken at $t = 0.5T$, or the end of the downstroke. Note that the angle of attack is negative, effectively using the lift generated by this angle of attack to counteract the suction from the shedding vortices.

Chapter 6

Optimization and Flapping Parameter Design

As demonstrated in Chapter 5, we have found that making relatively modest changes to the shape of the angle of attack curve as function of time, $\alpha(t)$, can effectively mitigate unwanted unsteady effects, so optimizing $\alpha(t)$ can lead to a clean force generation with minimized cost σ^*. Additionally, the stroke angle β and Strouhal number St have strong effect on the resultant mean flapping forces. We therefore set up an optimization routine that optimizes the shape of the angle of attack as well as the Strouhal number and stroke angle.

More specifically, we parametrize the problem in terms of the following $N + 2$ parameters to be optimized:

- Stroke angle β
- Strouhal number St
- Trajectory of the angle of attack $\alpha(t)$ as function of time, over N equidistant time instances, which is splined to create a continuous function

6.1 Optimization Method

Our intent is to demonstrate that optimization can yield far superior performance, hence we chose from simple methodologies that are adequate to obtain results with relatively few experiments. More specifically, we employ a model-based optimization driving iterative experimental runs. Another reason for choosing this methodology is that a large number of discretization points N are needed to properly parameterize a trajectory, hence the number of optimization parameters is too large to search the entire parametric space for a global optimum within a reasonable number of experimental trials. For example, even a coarse discretization of $\alpha(t)$ into $N = 4$ parametric values, and then discretizing each of the $N + 2$ parameters into 10 values, results in 10^6 experiments.

Several studies have been performed with optimization routines guiding systematic experiments or CFD trials [12, 24], using algorithms such as weight perturbation [11] or CMA-ES [9]. However, these methods generally have far slower convergence when compared to model-based methods, where a theoretical model is used to guide the optimization between experimental trials. A disadvantage of model-based optimization is that the optimization engine can only make decisions informed by the model physics, which may not capture the full nature of the flow. The optimization may still reject disturbances from the unmodeled dynamics; however, it will only search in directions deemed favorable by the theoretical model.

Model-based optimization greatly improves the converge rate, since optimization gradients are calculated analytically instead of experimentally, but the optimality of the final result is dependent on the quality of the theoretical model. For the purposes of our design problem, however, the method is shown to design flaps that perform far better than the simple sinusoids described previously in Section 3.2.

The optimization algorithm is therefore organized as follows:

1. An initial flap is chosen based on the theoretical model, that meets a mean force vector constraint $\mathbf{F}_{theoretical} = \mathbf{F}_{desired}$, while minimizing the cost function $J = \sigma^*$.

2. The initial flap is run through an experimental trial, recording the true forces $F_x(t)$ and $F_y(t)$.

3. The initial flap shape is corrected using the theoretical model to predict how changes in the parameter space will change the measured $F_x(t)$ and $F_y(t)$ to the desired values, again minimizing the cost function $J = \sigma*$.

4. Steps 2 and 3 are repeated until satisfactory convergence is obtained, defined in our case as when the measured force from the experiment is within 5% of the desired value $\mathbf{F}_{desired}$.

The choice of model-based optimization algorithm is dependent on the nonlinearity and sparsity of the theoretical model dependencies on the parameter space. For our optimization, we chose Sequential Quadratic Program for Nonlinear Constrained Optimization, or SNOPT, an algorithm described in Gill et al. [7]. The optimization code, along with its associated MATLAB wrapper, can be found at Philip Gill's website [7].

6.2 Theoretical Model Used in the Optimization

We use a relatively simple theoretical model based on a blend of two-dimensional, linear, unsteady thin-airfoil theory and a quasi-steady drag formulation:

$$\mathbf{F}(t) = [L_{qs}(t) + L_{wake}(t)]\hat{\mathbf{e}}_L(t) + F_{am_1}(t)\hat{\mathbf{e}}_1(t) + F_{am_2}(t)\hat{\mathbf{e}}_2(t) + D_{qs}(t)\hat{\mathbf{e}}_D(t) \quad (6.1)$$

These forces are illustrated in Fig. 6-1. The quasi-steady lift $L_{qs}(t)$ is given by Eqn 4.4, reprinted below, having direction $\hat{\mathbf{e}}_L(t)$, which is perpendicular to the velocity $\mathbf{v}(t)$, and in the direction of the angle of attack:

$$\begin{gathered} L_{qs}(t) = \tfrac{1}{2}\rho c v(t)\, 2\pi \left(v(t)\alpha(t) + \tfrac{c}{2}\dot{\theta}(t) \right) \\ \hat{\mathbf{e}}_L(t) \times \mathbf{v}(t) = 0 \end{gathered} \quad (6.2)$$

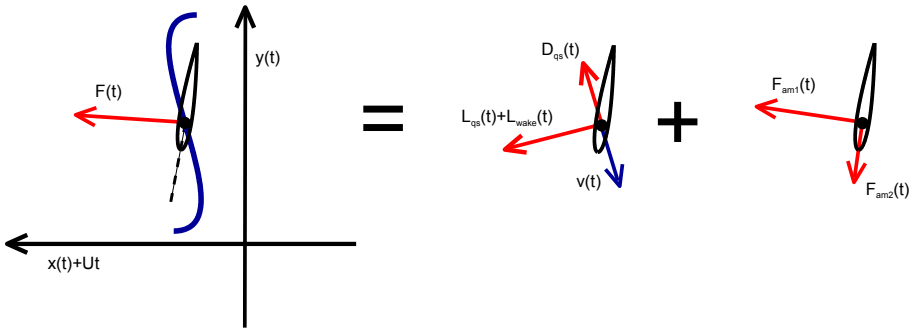

Figure 6-1: *Force Model* - The four components of the force model are illustrated above, along with their instantaneous directions. The lift and drag forces, $L_{qs}+L_{wake}$ and D_{qs}, are oriented with respect to the relative foil-fluid velocity, ignoring wake-induced velocities. The added mass forces, F_{am1} and F_{am2}, are represented in the foil body frame.

The wake-induced lift $L_{wake}(t)$ of a small-amplitude flaps is well studied in the flutter theory literature, based on the classic results of Theodorsen [32]. Unfortunately, the flapping motion discussed in this paper exceeds the linear range, since the amplitude of motion is comparable to the chord, $h/c = 1$, and there is unsteady in-line velocity, i.e. $\dot{v}_x \neq 0$. A more detailed analysis of the effects of the vortical patterns, such as the model described in Pan et al. [20], is therefore necessary to truly capture the wake effects.

To mitigate the computational complexity of these wake models, we consider the wake-induced lift as our prime unmodeled dynamic, and use a conservative simplification for the wake effects:

$$L_{wake}(t) \approx -\tfrac{1}{2} L_{qs}(t) \tag{6.3}$$

This simplification assumes that the Wagner effect [37] affects the lift magnitude for the entire flapping cycle, and ignores the phase information from the Theodorsen transfer function.

Hence, we proceed with the simplified model, because of its analytic tractability, and considered the omitted effects as unmodeled dynamics for the controller design.

The added mass effects are given in the body frame, using the unit vectors $\hat{\mathbf{e}}_1$ and $\hat{\mathbf{e}}_2$, where $\hat{\mathbf{e}}_1$ is parallel and $\hat{\mathbf{e}}_2$ is perpendicular to the foil chord. The magnitudes of

the added mass forces are:

$$\begin{aligned} F_{am_1}(t) &= v_2(t)\dot{\theta}(t)m_{22} \\ F_{am_2}(t) &= -a_2(t)m_{22} - a_\theta(t)m_{26} \end{aligned} \tag{6.4}$$

where v_2, a_2, and a_θ denote the global linear velocity, linear acceleration, and angular acceleration, respectively, expressed in the body frame of the unit vectors $\hat{\mathbf{e}}_1$ and $\hat{\mathbf{e}}_2$. The added mass coefficients are approximated by a plate rotated at its quarter chord, namely:

$$\begin{aligned} m_{22} &= \tfrac{1}{4}\rho\pi c^2 \\ m_{26} &= -\tfrac{1}{16}\rho\pi c^3 \end{aligned} \tag{6.5}$$

The drag force is approximated by a quasi-steady drag equation, oriented in the direction $\hat{\mathbf{e}}_D(t)$, opposing the instantaneous velocity, with magnitude:

$$D_{qs}(t) = \frac{1}{2}\rho c v(t)^2 C_D(\alpha) \tag{6.6}$$

where the coefficient of drag $C_D(\alpha)$ is approximated by a polynomial fit of measured steady drag force on the foil, illustrated in Fig. 6-2:

$$C_D(\alpha) = -3.70\alpha^6 + 2.08\alpha^4 + 2.52\alpha^2 + 0.0334 \tag{6.7}$$

We do not use a polynomial fit for the coefficient of lift C_L, since using the steady lift coefficient is a poor predictor of dynamic stall effects. Instead as mentioned above in Eqn 6.2, we use an unsteady linear approximation for the lift coefficient and include a magnitude correction for wake effects.

6.3 Optimization Constraints

To automatically design flaps that meet all design criteria, we implement a number of constraints to guide the optimization routine, as follows:

1. The mean of the predicted force component parallel to the direction of the

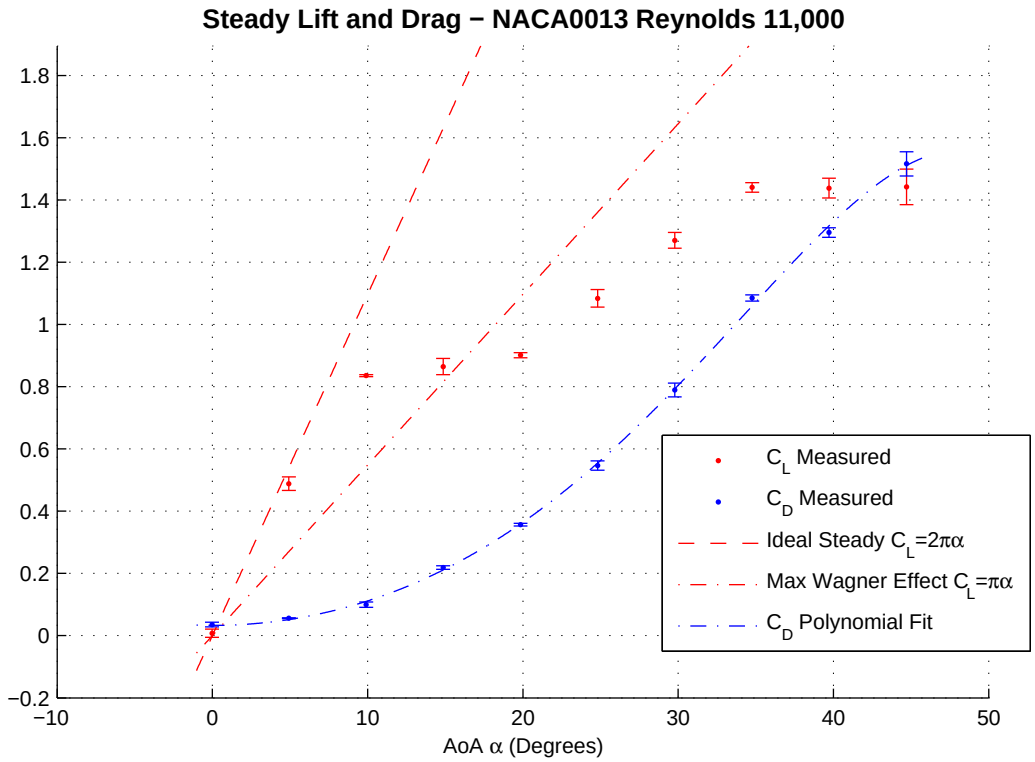

Figure 6-2: *Steady Force Measurements on NACA0013 Foil* - Force data as the NACA0013 foil is towed at constant speed, averaged over three trials of 20 chord-lengths of travel. The drag data is fit to a polynomial for use in the theoretical drag model. The lift data is not fit to a polynomial, as the steady lift coefficient is a poor predictor of unsteady lift at high angle of attack. The theoretical lift coefficient is $C_L = 2\pi\alpha$, but we instead use $C_L = \pi\alpha$ to give a conservative approximation of wake effects, as predicted by Wagner's impulsive foil theory [37].

desired force, $F_{\parallel}(t)$, is within 1% of the desired force magnitude.

2. The mean of the predicted force component perpendicular to the direction of the desired force, $F_{\perp}(t)$, is less than 1% of the desired force magnitude.

3. The jerk of $\theta(t)$ stays below a target value that scales appropriately with the flapping frequency and number of discretizations of t. This is easily implemented by keeping the triple difference $|\theta_k - 3\theta_{k+1} + 3\theta_{k+2} - \theta_{k+3}|$ under a maximum value. For our optimizations, we set this maximum value at $1/N$, in order to generate highly smooth motion trajectories.

4. The angle of attack $\alpha(t)$ must avoid full stall. In general, we found that a

large α was necessary around $t = 0$ and $t = T/2$ to mitigate the additional lift caused from rotating the foil, while a smaller α was necessary during the rest of the trajectory. We therefore constrained the angle of attack between two offset cosine curves:

$$\begin{gathered} \alpha_{mid} = 25^\circ \quad \alpha_{turn} = 45^\circ \\ \alpha_{max}(t) = (\alpha_{turn} - \alpha_{mid})[\tfrac{1}{2} + \tfrac{1}{2}\cos(2\pi f t)] + \alpha_{mid} \\ \alpha_{min}(t) = (\alpha_{turn} - \alpha_{mid})[-\tfrac{1}{2} + \tfrac{1}{2}\cos(2\pi f t)] - \alpha_{mid} \end{gathered} \tag{6.8}$$

$$\alpha_{min}(t) < \alpha(t) < \alpha_{max}(t) \tag{6.9}$$

In addition, we filter the force data at a lower frequency for the optimization routine, using a 5th order low-pass Butterworth at 5 Hz. This filter removes the force signature of the Strouhal shedding from the boundary layer breakup, which occurs around 6 Hz. While the other forces on the foil can be mitigated by through the optimization by changing the angle of attack of the foil, the Strouhal shedding phenomena is unstable, meaning that changing the angle of attack of the foil will only flip the phase of the vortex shedding. The lower frequency filter therefore mitigates this issue and improves convergence of the model-based corrections.

6.4 Optimization Results Based on the Theoretical Model

We verify the model performance in two ways, by comparison of the model and experimental force measurements, and by noting the direction of the predicted gradients of the parameters with respect to the true optimum. The latter of these evaluations is more significant, because it is more important that the model predicts the correct direction, toward the optimum value, than providing a precise estimate of that optimal value.

First we obtain the optimum values using only the theoretical model outlined above in Section 6.2, i.e. without conducting an experiment. Results are illustrated

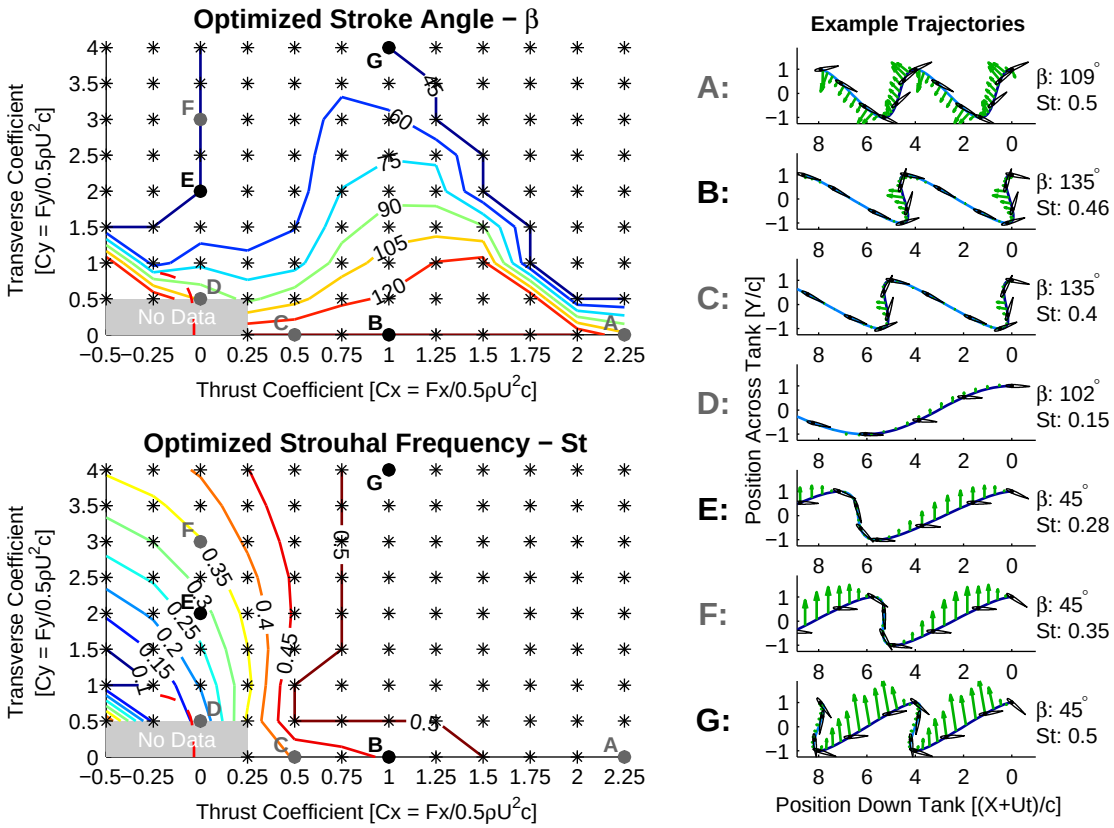

Figure 6-3: *Parameter Selection Using Only the Theoretical Model* - Optimized flapping patterns using the theoretical model only. A flapping pattern was derived for every asterisk in the colored plot, based on 52 parameters (stroke angle β, Strouhal number St, and 50 equidistant time intervals for the angle of attack over one period $\alpha(t)$). The upper left contour plot indicates the stroke angle β, with red implying backwards, turtle-like in-line motion; while blue is for forward, bird-like in-line motion. The lower left contour plot indicates the designed flapping frequency. A few of the designed trajectories are illustrated along right border of the figure, indicating their β, St, $\alpha(t)$, and predicted force performance. The ideal polar for a NACA0013 in steady flow is given by the red dashed curve. Note that when the intended $C_y = 0$, the optimized trajectories have substantial backwards in-line motion. When larger transverse force is desired, trajectories with forward in-line motion are obtained. Near the NACA0013 steady flow polar, trajectories are optimized to have very low flapping frequency. Trajectories B, E, and G are further optimized using experiments in Section 7.

in Fig. 6-3, where the contour plots provides the value of the stroke angle β and Strouhal number St as function of the required thust and transverse force coefficients, C_x and C_y, respectively. The flapping pattern is defined by the same parameters as given in Eqn 3.7, except that instead of limiting the angle of attack as function of time, $\alpha(t)$, to a simple harmonic, it is instead parametrized by $N = 50$ equidistant time instants over one period of the flapping motion.

First, we note that optimized flaps for zero transverse force, i.e. along the $C_y = 0$ axis, require substantial backwards in-line motion ($\beta > 90°$) when the thrust constraint is also low. As the thrust constraint increases, however, it becomes increasingly more difficult to use only a power downstroke, without violating the angle of attack constraint. As a result, the optimization chooses increasingly more symmetric profiles, which incur higher oscillation costs. This result is in agreement with Licht et al. [15], where backwards in-line motion was also found to decrease the mean thrust.

As the required transverse force coefficient, C_y, increases, the model predicts increasingly larger forward flaps ($\beta < 90°$), capturing the features of bird-like flapping noted by Tobalske and Dial [33].

The model also predicts the gliding regime, indicated by the red dashed polar, which shows the performance of a NACA0013 foil in steady flow. As the intended C_x and C_y approach this regime, the predicted ideal Strouhal number decreases dramatically, as indicated by the slow flaps in the lower left corner of Fig. 6-3. The parametrization, however, eventually breaks down at such low Strouhal numbers - as St approaches zero, β no longer affects the flap - so the predicted ideal stroke angle varies erratically.

Chapter 7

Optimization Results Using Experiments

We proceed to derive optimized flapping patterns as outlined in Section 6.1, i.e. using first the results of the theoretical model from the previous section, and then testing the foil experimentally. Based on an assessment of the experimental performance of the foil, we use the model to provide a new estimate, and continue alternating between experiments and model-based corrections, until convergence is obtained. As such, we take the results from Optimizations B, E, and G in Fig. 6-3, and further optimize them using experiments to design Trajectories IV, V, and VI respectively.

7.1 Optimized Trajectory IV - Intended $C_x = 1$ $C_y = 0$

An example optimization progression for a thrust-producing flap is illustrated in Fig. 7-1, with required mean thrust coefficient $C_x = 1$ and transverse force coefficient $C_y = 0$.

The initial flapping pattern, taken from Optimization B of Fig. 6-3, provides results in the right direction, but the unaccounted effects provide a relatively large mean C_y. It should be noted that this initial flap performs far better than the simple

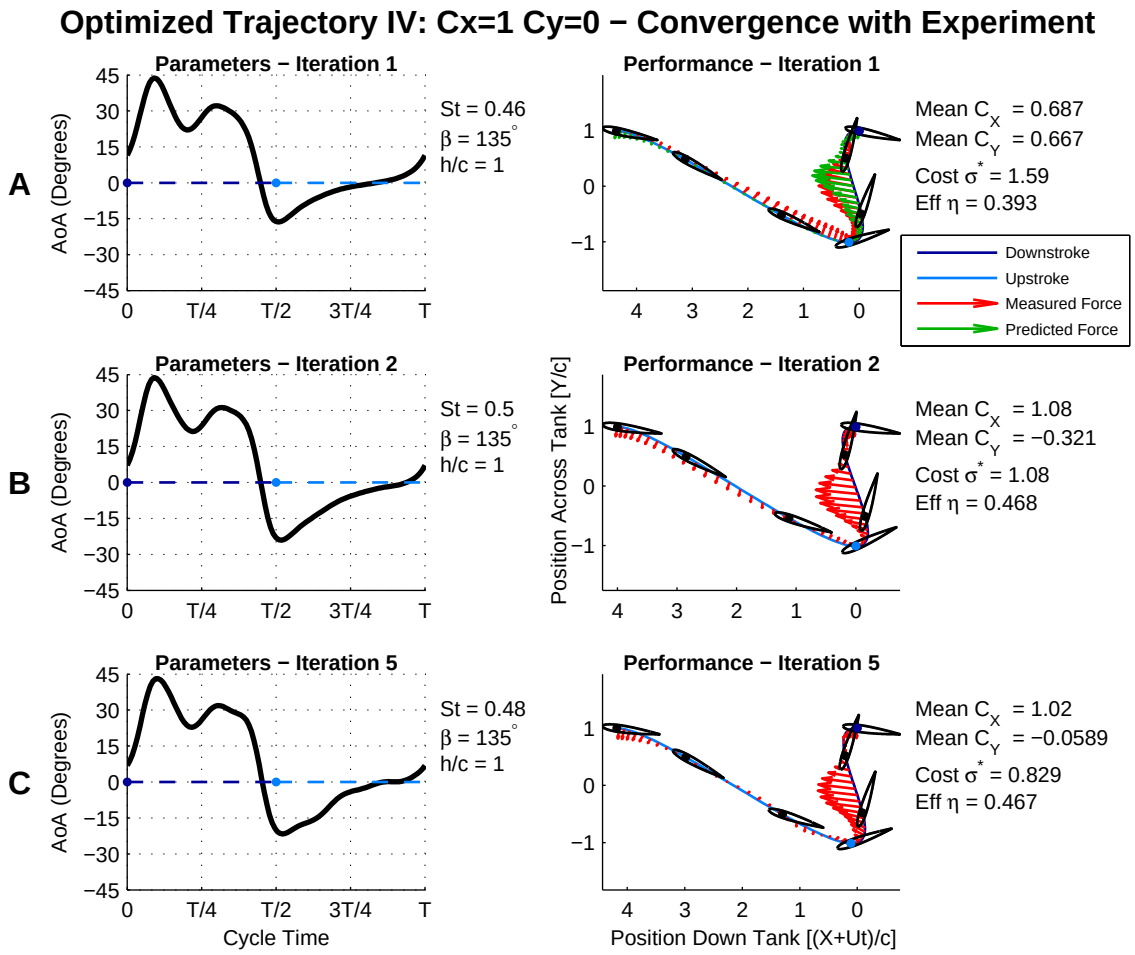

Figure 7-1: *Optimization IV Using Experiments* $C_x = 1$ $C_y = 0$ - Each row of the figure refers to an iteration of the optimization process. **A:** The optimization begins with the results of Fig. 6-3, designed for the required $C_x = 1$ and $C_y = 0$. The flapping motion and resulting forces are shown in the upper left plot, with green depicting the expected force from the model, and red the force measured from the experiment. **B:** On the basis of the difference between measured and predicted force, a new flap is designed, which is shown in the middle plots. **C:** After five such iterations, the force performance has suitably converged.

in-line motion flaps described in Section 4.3. Compared to the flap in Fig. 4-3, the angle of attack has been altered to mitigate much of the unwanted lift at the beginning and end of the downstroke, indicated by the peaks and troughs in the angle of attack $\alpha(t)$, largely restricting the lift to the middle region of the downstroke. The overall mean force, however, has a large bias towards positive C_y since the model does not adequately predict the wake-induced lift.

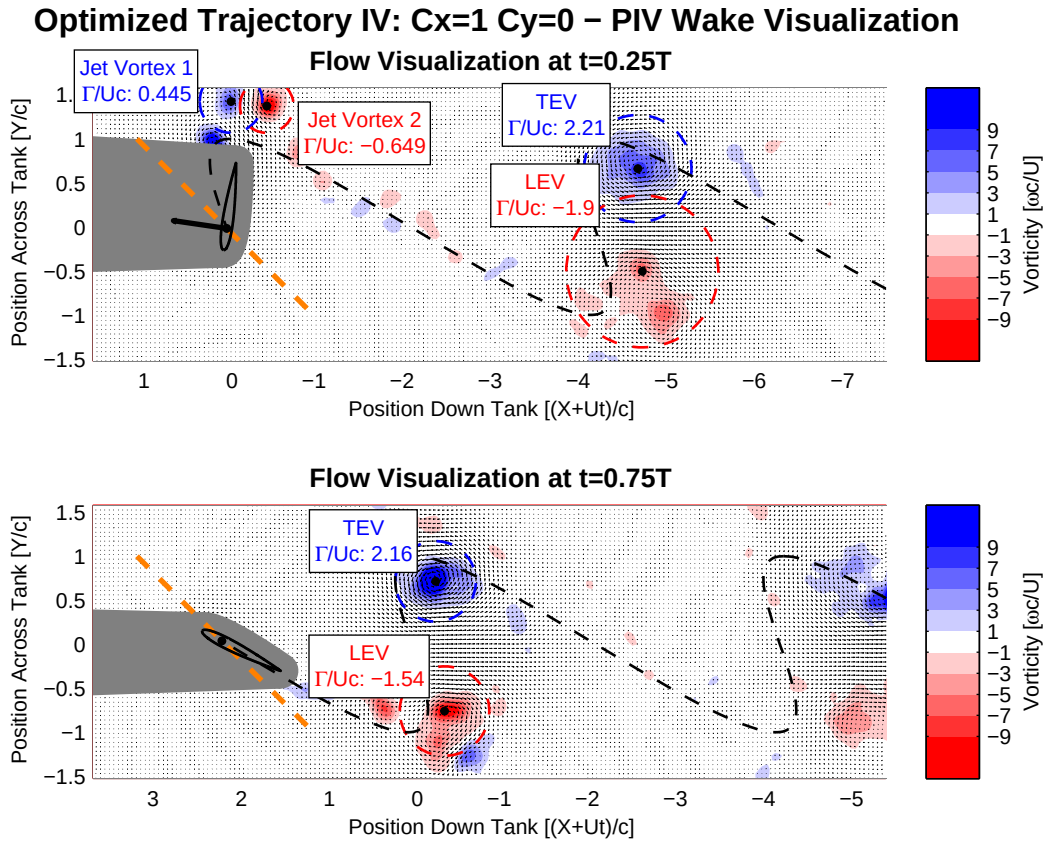

Figure 7-2: *Flow Visualization on Optimized Trajectory IV* $C_x = 1$ $C_y = 0$ - The phase-averaged PIV data illustrates the wake structure at $t = 0.25T$ (midway through the downstroke) and $t = 0.75T$ (midway through the upstroke). The shadow of the foil in the laser plane is colored in gray, in addition to a conservative two interrogation-window region around the foil. The stroke plane, which moves to the left at velocity U is highlighted by an orange dashed line, while the black dashed line indicates the trajectory of the foil. The black arrow coming out of the foil quarter-chord point is the instantaneous fluid force, scaled by a force coefficient of 10 per chordlength of arrow. Note the dual jets, one formed between the two vortices shed when the foil rotates quickly and a second formed between the LEV and TEV that creates the pulsed thrust.

By assessing the difference between the predicted and experimentally measured forces, the theoretical model is used to provide a correction to the original design, which is assessed again, and a new correction is obtained. For example, the second designed flap mitigates most of the unwanted C_y (Fig. 7-1B). After five iterations of

experimental runs and model-based corrections, the design converges to within 5% of the desired mean force.

Fig. 7-2 gives a detailed view of the wake of this final optimized trajectory, obtained from phase-averaged PIV data. The number of datasets averaged ranges from four on the far left and right edges of the PIV image, to eight datasets in the center. As the foil rotates quickly at the beginning of the downstroke, a small jet of fluid is flung upwards, bound by two vortices. A trailing edge vortex (TEV) is shed as the foil accelerates into the downstroke, consistent with Wagner theory [37]. The leading-edge vortex (LEV) is shed at the end of the downstroke. These leading and trailing edge vortices form a rearward facing pulsed jet, providing a large thrust force with very little transverse force.

Circulation values demonstrated in Fig. 7-2 are calculated by summing all the vorticity of the same sign contained within a circular region, effectively allowing for overlapping regions of opposite-signed vorticity. These circular regions are centered on a local maximum or minimum in the vorticity field, and are radially dilated until the mean vorticity on the perimeter is 5% of the vorticity in the center [6].

7.2 Optimized Trajectory V - Intended $C_x = 0$ $C_y = 2$

Analogously to the motion profile designed in the previous section, the theoretical model is used to provide incremental corrections to experimental results, eventually converging to a motion trajectory with the intended mean force of $C_x = 0$ and $C_y = 2$.

As illustrated in Fig. 7-3, the theoretical model in Optimization E initially underestimates the downstroke lift, but otherwise accurately predicts the force performance. In this case, we follow a slightly longer convergence, eleven trials, to allow the optimization to get as close as possible to zero mean thrust.

The PIV wake visualization of this optimized trajectory is provided in Fig. 7-4. Similar to the previous optimized trajectory, a trailing-edge vortex is shed as the foil

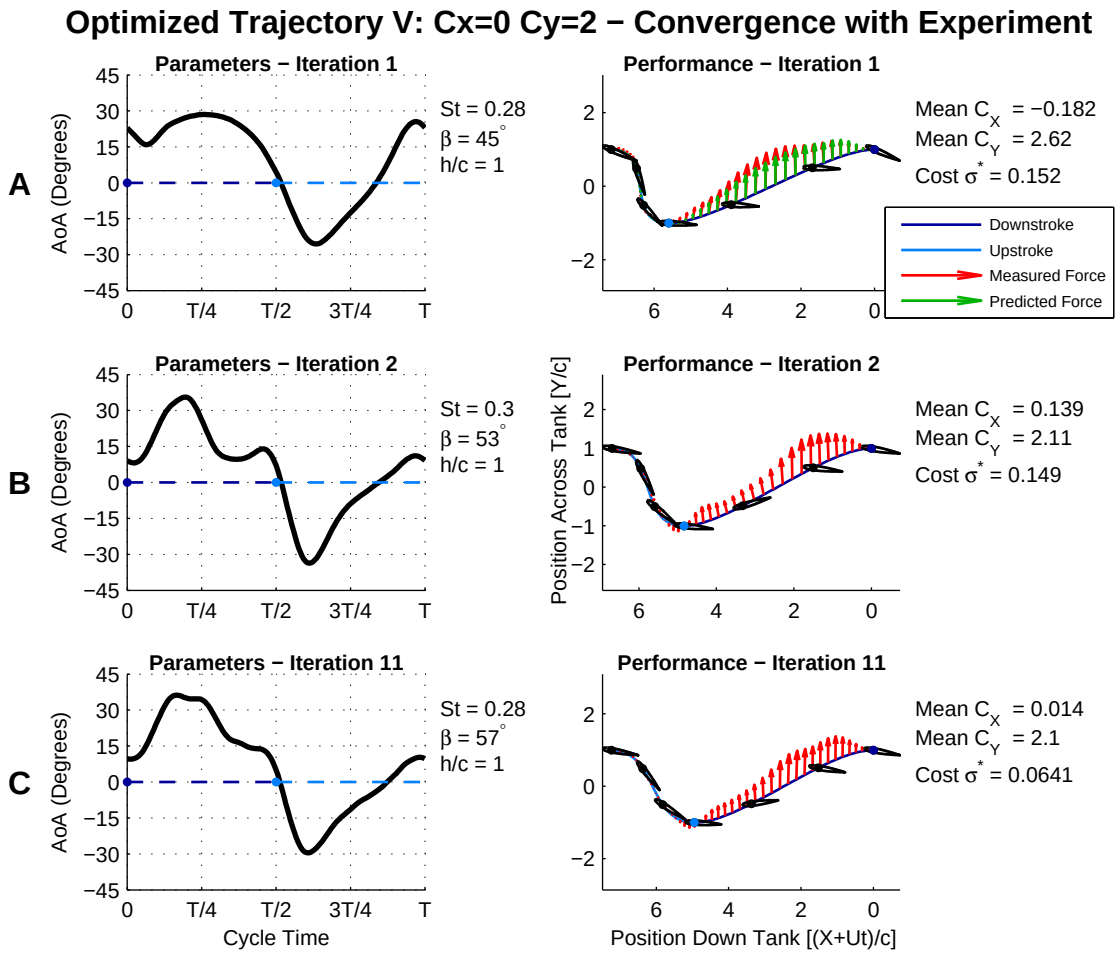

Figure 7-3: *Optimization V Using Experiments* $C_x = 0$ $C_y = 2$ - Similar to Fig. 7-1, each row of the figure refers to an iteration of the optimization process. **A:** The top row indicates the flap designed through the model-only optimization described in Fig. 6-3. In this case, the routine initially underestimates the lift during the downstroke. **B:** On the basis of the difference between measured and predicted force, a new flap is designed. **C:** After a number of such iterations, the force performance has suitably converged.

accelerates into the downstroke. A bound leading edge vortex provides a large lift force, which is then shed at the end of the downstroke. This leading edge vortex disperses relatively quickly, aided by the trailing-edge shedding at the beginning of the upstroke.

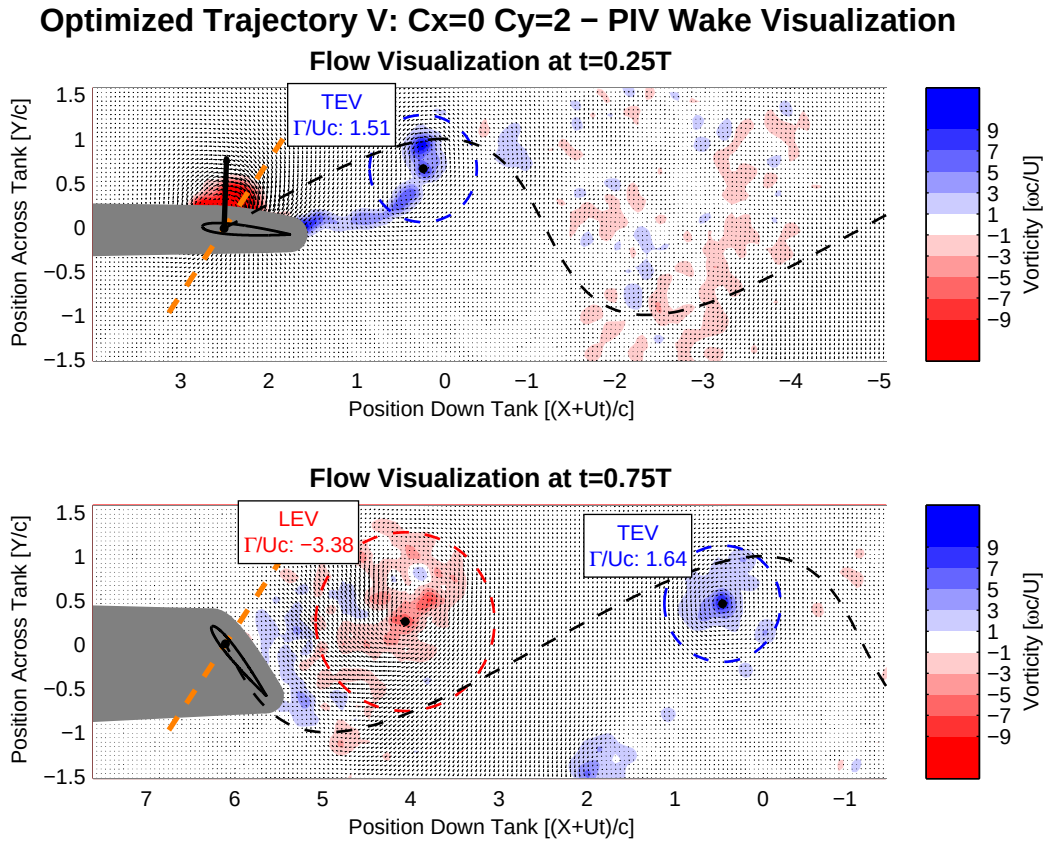

Figure 7-4: *Flow Visualization on Optimized Trajectory V* $C_x = 0$ $C_y = 2$ - Similar to Fig. 7-2, the gray region indicates PIV data invalidated by the laser shadow and proximity to the foil. The orange and black dashed lines indicate the stroke plane and position history of the foil respectively. Note the large leading edge vortex structure midway through the downstroke, as well as a trailing-edge vortex shed at the beginning of the downstroke.

7.3 Optimized Trajectory VI - Intended $C_x = 1$ $C_y = 4$

Fig. 7-5 demonstrates one final optimized trajectory with intended thrust coefficient of $C_x = 1$ and transverse coefficient of $C_y = 4$. This final experiment uses Optimization G of Fig. 6-3 as an initialization before improving the force performance.

This trajectory particularly highlights the importance of in-line motion for aug-

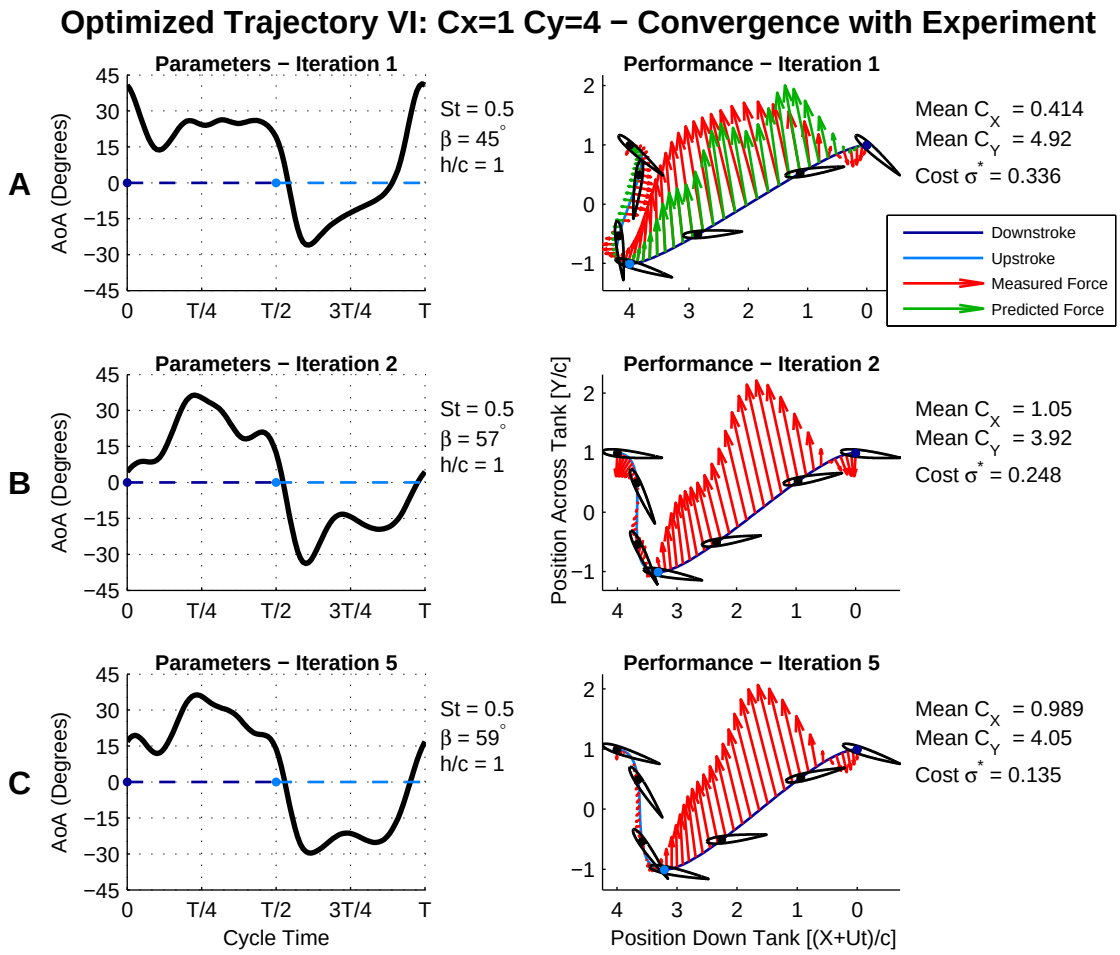

Figure 7-5: *Optimization VI Using Experiments* $C_x = 1$ $C_y = 4$ - Similar to Fig. 7-1, each row of this figure refers to an iteration of the optimization process. **A:** The top row indicates the flap designed through the model-only optimization described in Fig. 6-3. In this case, the routine initially underestimates the lift during the downstroke and ignores wake effects during the upstroke (top plots). **B:** After five iterations of improving the experiment based on the difference between the measured and predicted force, the mean force converges (**C**).

menting the foil lift. For example, a lift coefficient of $C_L = 4$ is not possible on a typical steady foil - assuming the ideal $C_L = 2\pi\alpha$, a steady foil would require an angle of attack of $\alpha = 36°$, which is well-beyond the stalling angle. Lift augmentation in this case is possible because of the in-line motion, which allows the foil to move faster than the mean flow, in addition to delayed stall effects from the pulsed angle of attack.

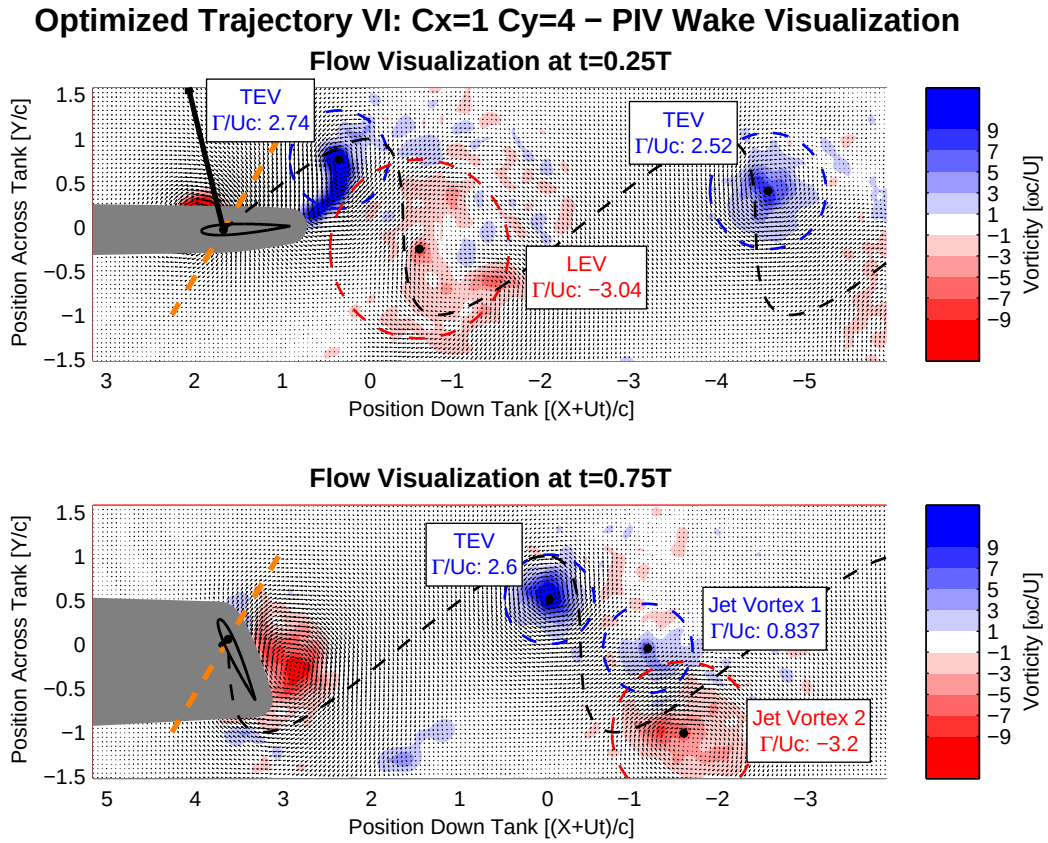

Figure 7-6: *Flow Visualization on Optimized Trajectory VI* $C_x = 1$ $C_y = 4$ - The PIV data is phase averaged at $t = 0.25T$ and $t = 0.75T$, or the middle of the downstroke and the middle of the upstroke. The foil trajectory in the global frame is indicated by the dashed black line, while the stroke plane is indicated by the dashed orange line. Note the staggered trailing and leading edge vortices, with the LEV augmenting the downstroke lift. The TEV indicates that there is bound vorticity during the downstroke, while the small jet illustrates the generated thrust.

As indicated in Fig. 7-5, the optimization routine again underestimates the downstroke lift, but converges suitably after a number of corrections to the original experiment. The foil wake is demonstrated in Fig. 7-6. Similar to the previous wake, this wake consists of staggered leading and trailing edge vortices, with the trailing edge vortex shedding as the foil accelerates into the downstroke and the bound leading edge vortex augmenting the lift during the downstroke.

Additionally, we can see a smaller vortex above the shed LEV, forming a jet flow. This jet indicates that thrust has been generated during the downstroke, analogous to how the TEV indicates the existence of bound vorticity on the foil that provides the lift.

Chapter 8

Conclusions and Future Work

8.1 Force Performance

Birds and certain marine animals actuate their flapping foils with in-line motion, and experiments have demonstrated that in-line motion can improve force vectoring and control without necessarily sacrificing efficiency [15]. In-line oscillation is associated with a power downstroke and a feathering upstroke. Depending on the direction of the in-line motion during the downstroke, the resulting force can be made to consist of mainly a thrust force with small oscillatory lift, as in turtles and mollusks, or to consist of a large lift component in addition to thrust, as in a bird. The ratio of thrust to lift force can be chosen arbitrarily by adjusting the in-line motion.

In the case of large thrust generation, we show that the principal restriction is in the maximum angle of attack to prevent excessive dynamic stall. Although the maximum angle of attack is significantly higher than the stalling angle for a foil moving at constant angle of attack, a reasonable upper limit still exists. Hence, as the specified thrust force is increased, optimization tends increasingly towards a symmetric flapping, i.e. involving little in-line motion and a power upstroke.

In the case of large lift generation, forwards in-line motion can be used to increase the mean lift far beyond the steady foil case. The high pulsed angle of attack does not stall due to delayed stall effects, while the increased effective foil velocity further boosts the lift. This extra lift could be especially useful for engineering applications

of unsteady foils.

Added complexity results from the in-line motion, both in terms of having an extra degree of freedom to actuate and because several parameters need to be optimized: The overall motion, even under steady-state conditions, is not purely sinusoidal, while strong effects from the vortical patterns in the wake require additional modification of the motion profile. Such optimization is especially required when a low lift force is commanded. The overall force is very sensitive to the functional shape of the angle of attack as unsteady wake effects become dominant, because of the large difference in relative velocity between the downstroke and upstroke.

I show in this thesis that such an optimization scheme is possible by employing a model-based iterative optimization method. A simplified theoretical force model is used to drive an iterative process, altering the parameters of the flapping foil trajectory based in the difference between the theoretical predictions and experimental results. The process is shown to converge, leading to the generation of forces in the desired direction and with very small undesirable forces. The parameters of the trajectory consist of the Strouhal number, stroke angle, and the profile of the angle of attack as function of time; the latter is specified at N points along one period of oscillation, where typically $N = 50$. Three examples of optimized flapping foils have been worked in detail:

- Trajectory IV, a turtle-like case, with specified thrust coefficient $C_x = 1$, and zero lift coefficient $C_y = 0$;

- Trajectory V, a purely lifting foil, with zero specified thrust coefficient $C_x = 0$, and lift coefficient $C_y = 2$; and

- Trajectory VI, a bird-like case, with specified thrust coefficient $C_x = 1$ and lift coefficient $C_y = 4$.

The present results have been derived for steady-state oscillations, and for oscillations that transition smoothly from cycle to cycle (Fig. 1-2). However, the same procedure can be extended to apply to rapidly varying motion, such as needed for maneuvering.

As noted in Section 4, Trajectories I, II, and III represent un-optimized examples using simple sinusoidal definitions for the motion trajectory.

8.2 Characteristic Wakes

The wakes of asymmetric motion profiles vary substantially from the classic reverse von Kármán wake of a symmetrically flapping foil. The in-line motion adds further variability to the wake.

In Trajectory IV, the turtle-like case designed to produce only thrust force $C_x = 1$, the wake consists of two large counter-rotating vortices placed along a single transverse line (Fig. 7-2). This wake is analogous to a pulsed jet or the drag-based thrust from a paddle, yet the force remains lift-based and efficient because the in-line motion rotates the effective foil velocity. Small additional vortices can also be shed as the foil quickly rotates at the beginning of the downstroke. The optimization process minimizes the strength of secondary vortices primarily through changes in the angle of attack profile.

In Trajectory V with $C_x = 0$ and $C_y = 2$, a bird-like forwards moving downstroke, the wake consists of one TEV that sheds as the foil accelerates into the downstroke, and a strong LEV that boosts the lift and sheds at the end of the downstroke. The TEV is indicative of some bound foil vorticity. These two vortices are staggered asymmetrically in the wake because of the in-line motion.

Trajectory VI with $C_x = 1$ and $C_y = 4$ corresponds to substantial transverse force combined with a small thrust force. This wake combines the features of Trajectory IV and V. A small vortex forms transverse to the shed LEV, forming a rearward-facing jet that indicates the presence of an upstream thrust force (Fig. 7-6). If no thrust is desired, as in Trajectory V, the pair instead annihilates and no jet forms (Fig. 7-4 Top).

8.3 Future Work

8.3.1 Real-Time Force Control

The controller from Chapter 5 has not been tested in experiment, given that the optimization routine is a better definition of the model-uncertainly problem. However, a controller would be necessary for rejecting flow disturbances, such as placing the flapping foil within a large von Kármán vortex street or a flow of unsteady direction. A real-time controller, following a baseline trajectory developed by the optimization routine, would be a valuable addition to this work. Given a baseline trajectory, more traditional time-varying control solutions could also be used, such as a time-varying linear quadratic regulator (TVLQR), to mitigate the variable gain between the angle of attack and lift caused by the changing foil velocity.

8.3.2 Three-Dimensional Effects

This work has so far been limited to the two-dimensional flapping foil problem, where the foil is simply translated and pitched in a single plane. However, most examples of flapping foils are strongly three-dimensional, such as a pitching and rolling bird wing that extends from the animal's body.

Various simple extensions exist from the planar theory into the true three-dimensional problem, such as the 70% foil span approximation from propeller theory [31]. Adding in-line motion, or yaw, to the three-dimensional flapping flight problem would be a necessary extension of this work for the development of a flapping foil vehicle.

8.3.3 Applications on a Flapping Foil Vehicle

In-line motion has numerous applications if implemented on a traditional flapping foil vehicle:

- Position Trajectory Following - The ability to easily and repeatedly vector the force from a flapping foil improves the vehicle's ability to follow a sharply maneuvering trajectory.

- Augmented Lift Maneuvers - A flapping foil with in-line motion can generate huge coefficients of lift (see Section 7.3). This ability could give a vehicle designed for gliding, i.e. large aspect ratio, the ability fly slower than the steady stall speed.

- Augmented Roll Rate - A flapping foil vehicle with in-line motion could also use the boosted lift coefficient to quickly roll the vehicle. Traditionally, fast roll rates are created using a wingaron, where the entire wing is used as an aileron. In-line motion can alternatively generate large impulsive roll rates by lunging the ailerons forwards instead of pitching the whole wing. Such a scheme could simplify the design of the wing.

Funding

I wish to acknowledge fiscal support from SMART, the Singapore-MIT Alliance for Research and Technology, within the CENSAM program; and from the MIT Sea Grant Program. I further wish to acknowledge fellowship support from the NSF Graduate Research Fellowships Program. This research was also conducted with Government support under and awarded by DoD, Air Force Office of Scientific Research, National Defense Science and Engineering Graduate (NDSEG) Fellowship, 32 CFR 168a.

Appendix A

Wake Visualization on Trajectories I,II, and III

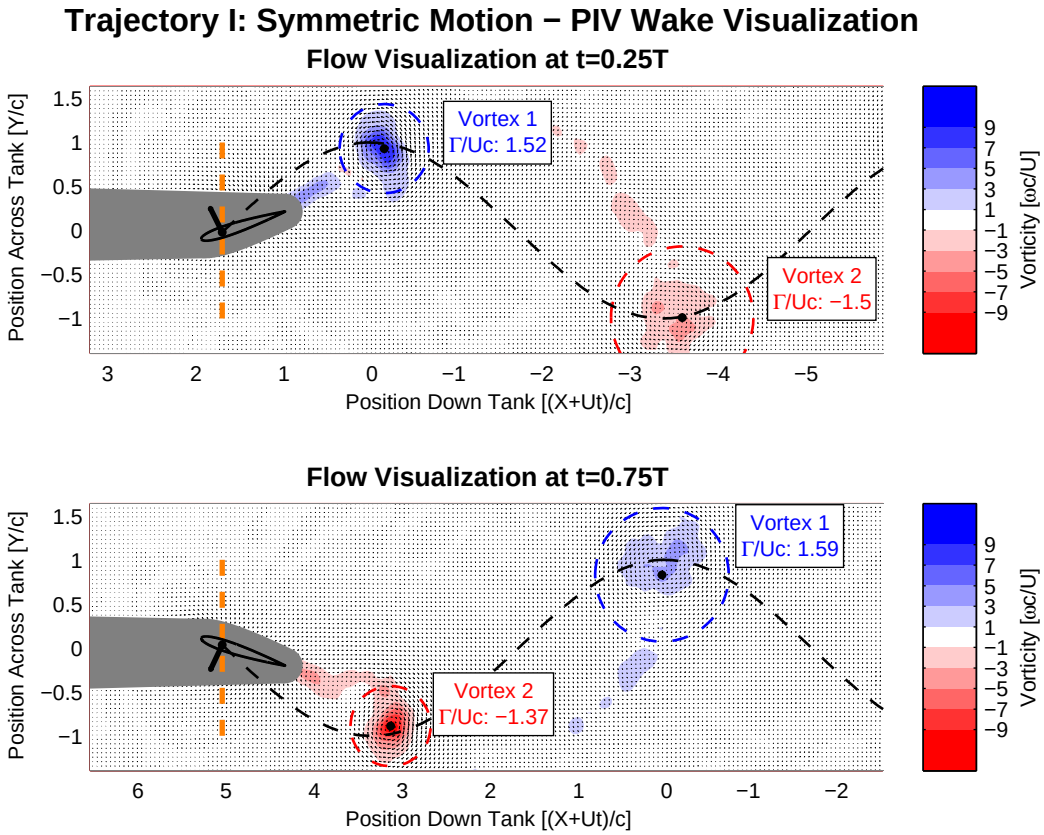

Figure A-1: *Flow Visualization on Trajectory I: Symmetric Flapping Profile* - The phase-averaged PIV data illustrates the wake structure at $t = 0.25T$ (midway through the downstroke) and $t = 0.75T$ (midway through the upstroke). The shadow of the foil in the laser plane is colored in gray, in addition to a conservative two interrogation-window region around the foil. The stroke plane, which moves to the left at velocity U is highlighted by an orange dashed line, while the black dashed line indicates the trajectory of the foil. The black arrow coming out of the foil quarter-chord point is the instantaneous fluid force, scaled by a force coefficient of 10 per chordlength of arrow. Note the classic inverted von Kármán vortex street.

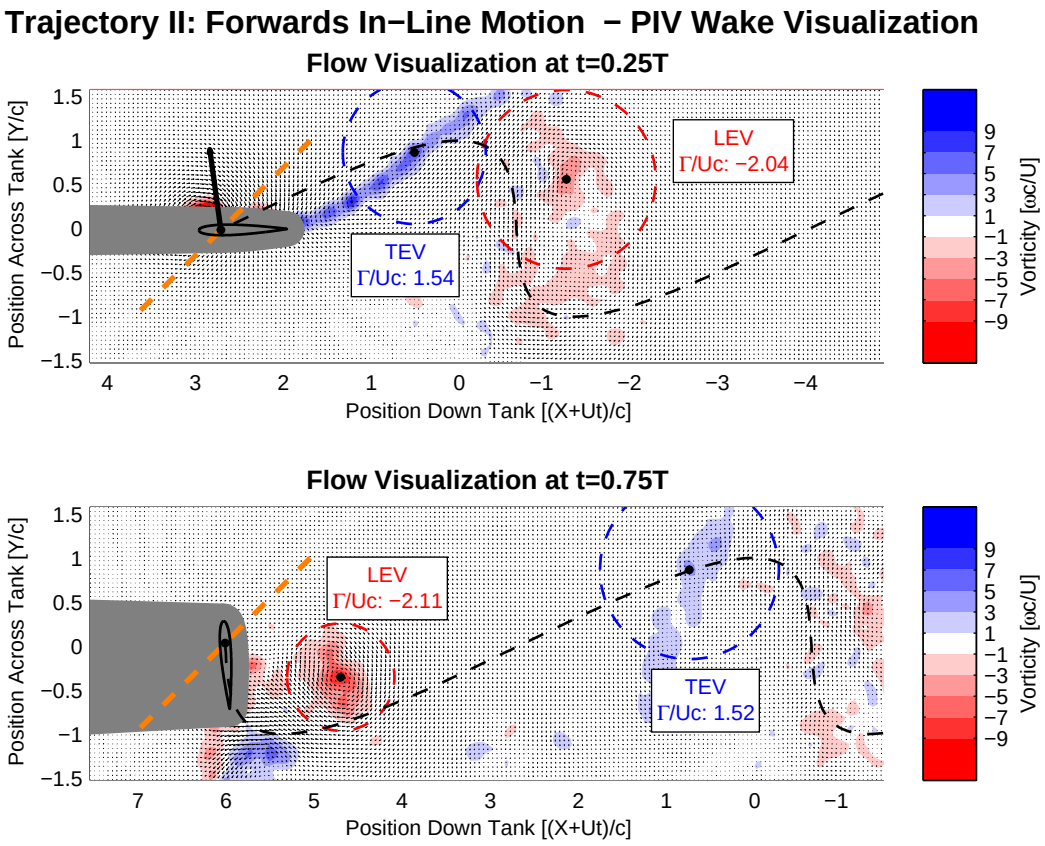

Figure A-2: *Flow Visualization on Trajectory II: Bird-Like Forward Biased Flap* - Similar to Fig. A-1, the gray region indicates PIV data invalidated by the laser shadow and proximity to the foil. The orange and black dashed lines indicate the stroke plane and position history of the foil respectively. Note the large leading edge vortex structure midway through the downstroke, as well as the set of trailing-edge vortices shed throughout the downstroke. The LEV is shed as the foil rotates into the upstroke, along with two smaller vortices that form a downwards-facing jet.

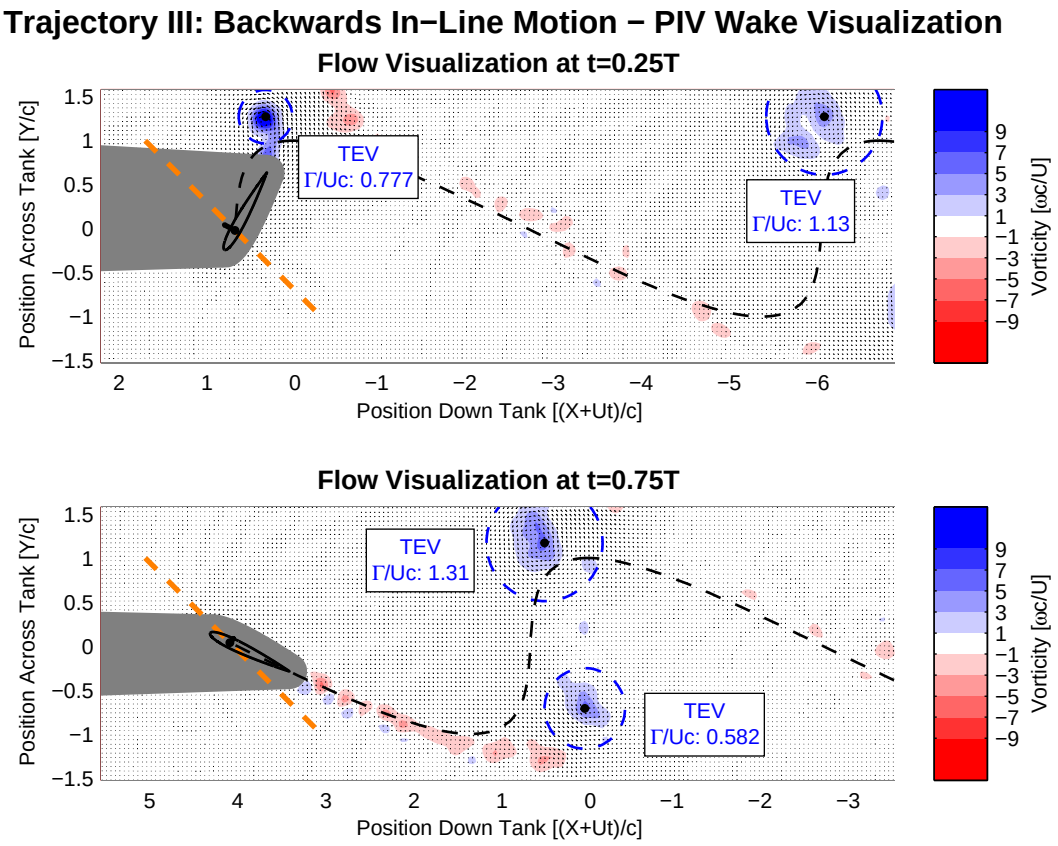

Figure A-3: *Flow Visualization on Trajectory III: Turtle-Like Backwards Biased Flap* - Similar to Fig. A-1, the gray region indicates PIV data invalidated by the laser shadow and proximity to the foil. The orange and black dashed lines indicate the stroke plane and position history of the foil respectively. Note two TEVs, one shed at the beginning and one shed at the end of the downstoke, and a trail of boundary layer breakup during the upstroke. This trajectory has very little net thrust, as indicated by the lack of a rearward facing jet behind the flap.

Bibliography

[1] J.M. Anderson, K. Streitlein, D.S. Barrett, and M. S. Triantafyllou. Oscillating foils of high propulsive efficiency. *Journal of Fluid Mechanics*, 360:41–72, 1998.

[2] Stephan E. Bansmer and Rolf Radespiel. Flapping Flight: High Thrust and Propulsive Efficiency due to Forward Gliding Oscillations. *AIAA Journal*, 50 (12):2937–2942, December 2012. ISSN 0001-1452. doi: 10.2514/1.J051749.

[3] Steven L Brunton and Clarence W Rowley. Empirical state-space representations for Theodorsen's lift model. *Journal of Fluids and Structures*, 38(0):174–186, 2013. ISSN 0889-9746. doi: http://dx.doi.org/10.1016/j.jfluidstructs.2012.10.005.

[4] J Davenport, Sarah A Munks, and P J Oxford. A comparison of the swimming of marine and freshwater turtles. *Royal Society for London. Series B, Biological Sciences*, 220(1221):447–475, 1984.

[5] Michael H Dickinson and KARL G Gotz. Unsteady aerodynamic performance of model wings at low reynolds numbers. *Journal of Experimental Biology*, 174 (1):45–64, 1993.

[6] Brenden P. Epps and Alexandra H. Techet. Impulse generated during unsteady maneuvering of swimming fish. *Experiments in Fluids*, 43(5):691–700, October 2007. ISSN 0723-4864. doi: 10.1007/s00348-007-0401-4.

[7] Philip E. Gill, Walter Murray, and Michael a. Saunders. SNOPT: An SQP Algorithm for Large-Scale Constrained Optimization. *SIAM Review*, 47(1):99–131, January 2005. ISSN 0036-1445. doi: 10.1137/S0036144504446096.

[8] Harish Gopalan and Alex Povitsky. Lift Enhancement of Flapping Airfoils by Generalized Pitching Motion. *Journal of Aircraft*, 47(6):1884–1897, November 2010. ISSN 0021-8669. doi: 10.2514/1.47219.

[9] N Hansen and a Ostermeier. Completely derandomized self-adaptation in evolution strategies. *Evolutionary computation*, 9(2):159–95, January 2001. ISSN 1063-6560. doi: 10.1162/106365601750190398.

[10] FS Hover, Ø Haugsdal, and MS Triantafyllou. Effect of angle of attack profiles in flapping foil propulsion. *Journal of Fluids and Structures*, 19(1):37–47, 2004.

[11] Marwan Jabri and Barry Flower. Weight Perturbation: An Optimal Architecture and Learning Technique for Analog VLSI Feedforward and Recurrent Multi-Layer Networks. *IEEE Transactions on Neural Networks*, 3:154–157, 1992.

[12] Stefan Kern and Petros Koumoutsakos. Simulations of optimized anguilliform swimming. *The Journal of experimental biology*, 209(Pt 24):4841–57, December 2006. ISSN 0022-0949. doi: 10.1242/jeb.02526.

[13] Gide Koekkoek, Florian T. Muijres, L. Christoffer Johansson, Melanie Stuiver, Bas W. van Oudheusden, and Anders Hedenström. Stroke plane angle controls leading edge vortex in a bat-inspired flapper. *Comptes Rendus Mécanique*, 340 (1-2):95–106, January 2012. ISSN 16310721. doi: 10.1016/j.crme.2011.11.013.

[14] Manoochehr M Koochesfahani. Vortical Patterns in the Wake of an Oscillating Airfoil. *AIAA Journal*, 27(9):1200–1205, 1989.

[15] S C Licht, M S Wibawa, F S Hover, and M S Triantafyllou. In-line motion causes high thrust and efficiency in flapping foils that use power downstroke. *The Journal of experimental biology*, 213(1):63–71, January 2010. ISSN 1477-9145. doi: 10.1242/jeb.031708.

[16] Ulla M Lindhe Norberg and York Winter. Wing beat kinematics of a nectar-feeding bat, Glossophaga soricina, flying at different flight speeds and Strouhal numbers. *The Journal of experimental biology*, 209(Pt 19):3887–97, October 2006. ISSN 0022-0949. doi: 10.1242/jeb.02446.

[17] Audrey P Maertens and Gabriel D Weymouth. Accurate Cartesian-grid simulations of fluid-body interactions at high Reynolds numbers. *To Be Submitted*, 2013.

[18] C. Maresca, D. Favier, and J. Rebont. Experiments on an aerofoil at high angle of incidence in longitudinal oscillations. *Journal of Fluid Mechanics*, 92(04):671, April 1978. ISSN 0022-1120. doi: 10.1017/S0022112079000823.

[19] Robert L Nudds, Graham K Taylor, and Adrian L R Thomas. Tuning of Strouhal number for high propulsive efficiency accurately predicts how wingbeat frequency and stroke amplitude relate and scale with size and flight speed in birds. *Proceedings. Biological sciences / The Royal Society*, 271(1552):2071–6, October 2004. ISSN 0962-8452. doi: 10.1098/rspb.2004.2838.

[20] Yulin Pan, Xiaoxia Dong, Qiang Zhu, and Dick K. P. Yue. Boundary-element method for the prediction of performance of flapping foils with leading-edge separation. *Journal of Fluid Mechanics*, 698:446–467, April 2012. ISSN 0022-1120. doi: 10.1017/jfm.2012.119.

[21] C J Pennycuick. Chapter 4 Vortices and Vortex Wakes. In C J Pennycuick, editor, *Modelling the Flying Bird*, volume 5 of *Theoretical Ecology Series*, pages 79–103. Academic Press, 2008. doi: 10.1016/S1875-306X(08)00004-X.

[22] P Prempraneerach, F S Hover, and M S Triantafyllou. The effect of chordwise flexibility on the thrust and efficiency of a flapping foil. In *Proc. 13th Int. Symp. on Unmanned Untethered Submersible Technology: special session on bioengineering research related to autonomous underwater vehicles, New Hampshire*, 2003.

[23] D A Read, F S Hover, and M S Triantafyllou. Forces on oscillating foils for propulsion and maneuvering. *Journal of Fluids and Structures*, 17:163–183, 2003.

[24] John W Roberts, Jun Zhang, and Russ Tedrake. From Motor to Interaction Learning in Robots. *From Motor to Interaction Learning in Robots*, pages 1–20, 2009.

[25] M. Rosen. *Experiments with swimming fish and dolphins*. American Society of Mechanical Engineers, New York, 1961.

[26] Anatol Roshko. Technical Report TN3169, On the Drag and Shedding Frequency of Two-Dimensional Bluff Bodies. Technical report, NACA, Washington DC, 1954.

[27] L Schouveiler, F Hover, and M Triantafyllou. Performance of flapping foil propulsion. *Journal of Fluids and Structures*, 20(7):949–959, October 2005. ISSN 08899746. doi: 10.1016/j.jfluidstructs.2005.05.009.

[28] A Slaouti and JH Gerrard. An experimental investigation of the end effects on the wake of a circular cylinder towed through water at low reynolds numbers. *Journal of Fluid Mechanics*, 112(1):297–314, 1981.

[29] Brett G Szymik and Richard a Satterlie. Changes in wingstroke kinematics associated with a change in swimming speed in a pteropod mollusk, Clione limacina. *The Journal of experimental biology*, 214(Pt 23):3935–47, December 2011. ISSN 1477-9145. doi: 10.1242/jeb.058461.

[30] Graham K Taylor, Robert L Nudds, and Adrian L R Thomas. Flying and swimming animals cruise at a Strouhal number tuned for high power efficiency. *Nature*, 425(October):707–711, 2003. doi: 10.1038/nature02047.1.

[31] Alexandra H Techet. Propulsive performance of biologically inspired flapping foils at high Reynolds numbers. *The Journal of experimental biology*, 211(Pt 2): 274–9, January 2008. ISSN 0022-0949. doi: 10.1242/jeb.012849.

[32] Theodore Theodorsen. General theory of aerodynamic instability and the mechanism of flutter. Technical report, Tech. Rep. 496, NACA, 1935.

[33] B Tobalske and K Dial. Flight kinematics of black-billed magpies and pigeons over a wide range of speeds. *The Journal of experimental biology*, 199(Pt 2): 263–80, January 1996. ISSN 1477-9145. doi: 10.1126/science.1178120.

[34] Bret W Tobalske, Douglas R Warrick, Christopher J Clark, Donald R Powers, Tyson L Hedrick, Gabriel a Hyder, and Andrew a Biewener. Three-dimensional kinematics of hummingbird flight. *The Journal of experimental biology*, 210(Pt 13):2368–82, July 2007. ISSN 0022-0949. doi: 10.1242/jeb.005686.

[35] G.S. Triantafyllou, M.S. Triantafyllou, and M.A. Grosenbaugh. Optimal Thrust Development in Oscillating Foils with Application to Fish Propulsion. *Journal of Fluids and Structures*, 7(2):205–224, 1993.

[36] M.S. Triantafyllou, G.S. Triantafyllou, and R. Gopalkrishnan. Wake mechanics for thrust generation in oscillating foils. *Physics of Fluids*, 3(12):28–35, 1991.

[37] Herbert Wagner. Über die entstehung des dynamischen auftriebes von tragflügeln. *ZAMM-Journal of Applied Mathematics and Mechanics/Zeitschrift für Angewandte Mathematik und Mechanik*, 5(1):17–35, 1925.

[38] G D Weymouth and Yue D K.P. Boundary data immersion method for Cartesian-grid simulations of fluid-body interaction problems. *J Comput Phys*, 230, 2011.

[39] G D Weymouth, D G Dommermuth, K Hendrickson, and D K P Yue. Advancements in Cartesian-grid methods for computational ship hydrodynamics. In *26th Symposium on Naval Hydrodynamics*, 2006.

[40] M S Wibawa, S C Steele, J M Dahl, D E Rival, G D Weymouth, and M S Triantafyllou. Global vorticity shedding for a vanishing wing. *Journal of Fluid Mechanics*, 695, February 2012.